Quiescent tumor cells shape the immunosuppressive microenvironment in pancreatic ductal adenocarcinoma

William Matsui

william.matsui@austin.utexas.edu

The University of Texas at Austin

Bryan McClellan

University of Texas at Austin https://orcid.org/0000-0003-2760-3939

Qiuju Wang

The University of Texas at Austin Dell Medical School

Kyaw Aung

Miami Cancer Institute, Baptist Health South Florida

Article

Keywords:

Posted Date: March 17th, 2026

DOI: https://doi.org/10.21203/rs.3.rs-8980750/v1

Additional Declarations: There is **NO** Competing Interest.

Quiescent tumor cells shape the immunosuppressive microenvironment in pancreatic ductal adenocarcinoma

McClellan, B.[1], Wang, Q.[1], Aung, K.[2], Matsui, W.[1]

[1] The University of Texas at Austin Dell Medical School, Department of Internal Medicine, Austin, TX, United States

[2] Miami Cancer Institute, Baptist Health South Florida, Miami, Florida, United States

Abstract

Immunotherapy, including chimeric antigen receptor (CAR) T-cell therapy, has limited activity in pancreatic ductal adenocarcinoma (PDAC). Using orthotopic PDAC mouse models, we identified a rare population of quiescent PDAC cells that increases after CAR-T cell therapy and exhibits relatively higher clonogenic growth and self-renewal potential than bulk tumor cells. These quiescent cells express high levels of Epiregulin (EREG), a secreted ligand for EGFR and ErbB4, and induce an immunosuppressive tumor microenvironment by increasing the frequency of ErbB4-expressing tumor-associated macrophages. Silencing EREG expression increased the sensitivity of both quiescent cells and tumors to CAR-T cells and improved relapse rates and overall survival. These findings demonstrate that rare quiescent tumor cells can modulate the tumor microenvironment in PDAC and suggest that EREG inhibition may enhance the efficacy of adoptive immunotherapeutic approaches in this disease.

Introduction

Pancreatic ductal adenocarcinoma (PDAC) is projected to be the second leading cause of cancer-related deaths in the United States by 2030 [1]. A major factor in these poor clinical outcomes is resistance to both cytotoxic chemotherapy and targeted agents. Similarly, immune checkpoint inhibitors have limited clinical activity, except in rare cases of PDAC with microsatellite instability (MSI) [2, 3]. Adoptive immunotherapy with CAR-T cells has demonstrated clinical efficacy in PDAC, but initial tumor responses are not sustained [4, 5]. Therefore, further insights into the mechanisms of resistance may lead to improved immune-based approaches for this disease.

Multiple mechanisms contribute to immunotherapy resistance in PDAC, including low neoantigen burden, the dense desmoplastic stroma, and the accumulation of immunosuppressive cell populations within the tumor microenvironment (TME) [6,7]. Myeloid-derived cells, particularly macrophages, are central to establishing and maintaining the immunosuppressive tumor microenvironment, thereby limiting the activity of both endogenous and adoptively transferred cytotoxic T cells [6-13]. While the immunosuppressive nature of the PDAC TME is well recognized, its adaptation to active anti-tumor immunity is not well understood. However, further insights into these changes may identify specific mechanisms and therapeutic targets to improve the durability of immune-based therapies.

Functionally distinct cell populations have been identified in PDAC with relatively enhanced clonogenic growth, tumor initiation, and metastatic potential compared to bulk tumor cells [14-17]. These properties suggest that cancer stem cells (CSCs) play a central role in tumor regrowth and progression [18]. Both normal adult stem cells and CSCs often reside in a quiescent state [19-24], which confers protection from immune surveillance by down-regulating MHC class I and NK cell-activating ligand expression [25-28]. Furthermore, quiescent cancer cells can actively promote local immune suppression within the TME by inducing hypoxia and recruiting immunosuppressive cells through secreted factors [25-27, 29, 30].

Given the intrinsic resistance of quiescent cancer cells, we developed a novel PDAC model to examine the impact of CAR T-cells targeting tumor cells in an MHC-independent manner [28, 31-33]. Using a live-cell quiescence reporter, we found that quiescent cancer cells with CSC properties are significantly enriched after CAR T-cell therapy. Quiescent cancer cells also expressed high levels of Epiregulin (EREG), an EGF-family ligand for EGFR/ErbB4 with established roles in normal tissue repair, regeneration, and inflammation [31, 34-38]. Further EREG expression is associated with low $CD8^+$ T-cell and high M2 macrophage infiltration in human PDAC [39]. EREG silencing in PDAC cells enhanced CAR T-cell activity, including improved targeting of quiescent tumor cells, reduced tumor regrowth, and extended survival. These EREG-mediated effects were dependent on $ErbB4^+$ macrophages, indicating that quiescent tumor cells orchestrate an immunosuppressive TME through macrophages and that targeting EREG may improve adoptive cell therapy in PDAC.

Materials and Methods

Cell culture

mT4-2D and KPC -/- murine PDAC cell lines were provided by David Tuveson and Cassian Yee at Cold Spring Harbor Laboratory and The University of Texas MD Anderson Cancer Center, respectively [40, 41] and maintained in DMEM with 10% FBS and 100 $\mu g\ ml^{-1}$ Primocin (Invivogen, antpm05). HEK 293FT cells were purchased from ATCC and cultured in DMEM with 10% FBS and 100 $\mu g\ ml^{-1}$ Primocin. Cells were tested for mycoplasma by PCR (Southern Biotech, 1310001) every 2 months and not passaged more than 15 times.

Patient-derived PDAC xenografts

PDAC surgical specimens were collected with written consent under the University of Texas at Austin IRB-approved-protocol (Protocol No. 2017060074). Patient-derived xenografts (PDX) were established and passaged in *Foxn1*$^{Nu/J}$ (Nude; strain no. 000819, Jackson Laboratory) mice, cryopreserved between passages F3-F6, and stored in liquid nitrogen.

Animals

All experiments were conducted within AAALAC guidelines and approved by the University of Texas Institutional Animal Care and Use Committee (Protocol No. IPROTO202500000255). C57/BL6J (strain no. 000664) and NSG (strain no. 005557) mice were either purchased from the Jackson Laboratory or bred in-house.

Molecular cloning and generation of DNA constructs

All cloning was performed using gBlocks from Integrated DNA Technologies (IDT) and NEB HIFI assembly master mix (New England Biolabs). All restriction enzymes used were from New England Biolabs. All plasmids were confirmed by NGS whole plasmid sequencing through plasmidsaurus (https://plasmidsaurus.com). To generate the human CD19 (hCD19) tdTomato-luc2 construct, the pCDH-EF1-luc2-P2A-tdTomato plasmid (Addgene, 72486) was digested with SalI-EcoRI and subjected to HIFI assembly with an hCD19 gBlock containing a 40 bp homology to the digested vector. The hCD19 sequence was obtained from MSCV-hCD19 (Addgene, 127889). To generate the p27k-mVenus-BlastR and p27k-miRFP670 constructs, part of the 2A sequence and puro resistance gene was removed from the p27k-mVenus plasmid (Addgene, 176651) with BamHI-SalI and replaced in frame with a gBlock containing a 40 bp homology with the T2A-BlastR cassette. The p27k-miRFP670 vector was constructed by digesting the p27k-mVenus vector with XbaI-EcoRV and assembling with a miRFP670 gBlock containing a 40 bp homology to the digested vector. Both sequences (BlastR and miRFP670) were obtained using Snapgene. All cloning schemes were first tested using the Snapgene NEB HIFI assembly tool.

Constitutive gene knockdown was carried out using shRNAs (Millipore Sigma): Non-target shControl: cat #: SHC016, GCGCGATAGCGCTAATAATTT; shEREG: cat #: TRCN0000250419, TGCGATGTGAGCACTTCTTTC; shNGF: cat #: TRCN0000351084, CCTGAAGCCCACTGGACTAAA; shSPRR1a: cat #: TRCN0000098406, CAACTGTCACTCCATCACCAT. Inducible EREG knockdown was carried out by cloning an EREG shRNA, TRCN00002419 (TGCGATGTGAGCACTTCTTTC), into the TetON-pLKO-puro vector (Addgene, 21915) using the manufacturer's protocol, except transforming plasmids into NEB stable competent cells instead of Stbl3. The scramble control shRNA (shScramble) was obtained from TetON-pLKO-puro-Scramble (Addgene, 47541).

The anti-hCD19 CAR vector was constructed using the CD19 scFV sequence (Addgene, 194457) derived from the anti-CD19 clone FMC63, and the anti-murine mesothelin scFV sequence was obtained from SS scFV [42]. To generate anti-mesothelin CAR T-cells expressing mTagBFP2, the eGFP gene was replaced with mTagBFP2 using a gBlock with sequence from Snapgene. Both scFV sequences for the murine CAR T-cells contain the same leader sequence and linkers followed by murine CD28 and CD3z endodomains as listed below:

anti-hCD19 scFV

ATGCTTCTCCTGGTGACAAGCCTTCTGCTCTGTGAGTTACCACACCCAGCATTCCTCCTGATCCCAG
ACATCCAGATGACACAGACTACATCCTCCCTGTCTGCCTCTCTGGGAGACAGAGTCACCATCAGTT
GCAGGGCAAGTCAGGACATTAGTAAATATTTAAATTGGTATCAGCAGAAACCAGATGGAACTGTT
AAACTCCTGATCTACCATACATCAAGATTACACTCAGGAGTCCCATCAAGGTTCAGTGGCAGTGG
GTCTGGAACAGATTATTCTCTCACCATTAGCAACCTGGAGCAAGAAGATATTGCCACTTACTTTTG
CCAACAGGGTAATACGCTTCCGTACACGTTCGGAGGGGGGACTAAGTTGGAAATAACAGGCTCCA
CCTCTGGATCCGGCAAGCCCGGATCTGGCGAGGGATCCACCAAGGGCGAGGTGAAACTGCAGGA
GTCAGGACCTGGCCTGGTGGCGCCCTCACAGAGCCTGTCCGTCACATGCACTGTCTCAGGGGTCTC
ATTACCCGACTATGGTGTAAGCTGGATTCGCCAGCCTCCACGAAAGGGTCTGGAGTGGCTGGGAG
TAATATGGGGTAGTGAAACCACATACTATAATTCAGCTCTCAAATCCAGACTGACCATCATCAAG
GACAACTCCAAGAGCCAAGTTTTCTTAAAAATGAACAGTCTGCAAACTGATGACACAGCCATTTA
CTACTGTGCCAAACATTATTACTACGGTGGTAGCTATGCTATGGACTACTGGGGTCAAGGAACCTC
AGTCACCGTCTCCTCAGCGGCCGCA

Anti-mesothelin scFV

ATGCTTCTCCTGGTGACAAGCCTTCTGCTCTGTGAGTTACCACACCCAGCATTCCTCCTGATCCCAA
TGCAGGTACAACTGCAGCAGTCTGGGCCTGAGCTGGAGAAGCCTGGCGCTTCAGTGAAGATATCC
TGCAAGGCTTCTGGTTACTCATTCACTGGCTACACCATGAACTGGGTGAAGCAGAGCCATGGAAA
GAGCCTTGAGTGGATTGGACTTATTACTCCTTACAATGGTGCTTCTAGCTACAACCAGAAGTTCAG
GGGCAAGGCCACATTAACTGTAGACAAGTCATCCAGCACAGCCTACATGGACCTCCTCAGTCTGA
CATCTGAAGACTCTGCAGTCTATTTCTGTGCAAGGGGGGGTTACGACGGGAGGGGTTTTGACTACT
GGGGCCAAGGGACCACGGTCACCGTCTCCTCAGGTGTAGGCGGTTCAGGCGGCGGTGGCTCTGGC
GGTGGCGGATCGGACATCGAGCTCACTCAGTCTCCAGCAATCATGTCTGCATCTCCAGGGGAGAA
GGTCACCATGACCTGCAGTGCCAGCTCAAGTGTAAGTTACATGCACTGGTACCAGCAGAAGTCAG
GCACCTCCCCCAAAAGATGGATTTATGACACATCCAAACTGGCTTCTGGAGTCCCAGGTCGCTTCA
GTGGCAGTGGGTCTGGAAACTCTTACTCTCTCACAATCAGCAGCGTGGAGGCTGAAGATGATGCA
ACTTATTACTGCCAGCAGTGGAGTGGTTACCCTCTCACGTTCGGTGCTGGGACAAAGTTGGAAATA
AAAGCGGCCGCA

mCD28

ATCGAGTTCATGTACCCCCCTCCCTACCTGGACAACGAGAGAAGCAACGGCACCATCATCCACAT
CAAAGAAAAGCACCTGTGCCACACCCAGAGCAGCCCCAAGCTGTTCTGGGCCCTGGTGGTGGTGG
CCGGCGTGCTGTTCTGTTACGGCCTGCTGGTCACAGTGGCCCTGTGCGTGATCTGGACCAACAGCA
GAAGAAACAGAGGCGGCCAGAGCGACTACATGAACATGACCCCCAGAAGGCCAGGCCTGACCAG
AAAGCCCTACCAGCCCTACGCCCCTGCCAGAGACTTCGCCGCCTACAGACCC

mCD3z

AGAGCCAAGTTCAGCAGATCCGCCGAGACAGCCGCCAACCTGCAGGATCCCAACCAGCTGTACAA
CGAGCTGAACCTGGGCAGACGGGAGGAATACGACGTGCTGGAAAAGAAGAGAGCCAGGGACCCC

GAGATGGGCGGCAAGCAGCAGAGAAGAAGAAACCCTCAGGAAGGCGTCTACAACGCCCTGCAGA
AAGACAAGATGGCCGAGGCCTACAGCGAGATCGGCACCAAGGGCGAGAGAAGAAGGGGCAAGG
GCCACGATGGCCTGTACCAGGGCCTGTCCACCGCCACCAAGGACACCTACGACGCCCTGCACATG
CAGACCCTGGC
CCCCAGATAA

The anti-human mesothelin CAR was assembled using the lentiviral expression vector pRRL.SIN.EF1A.CD19-FMC63.218.CAR-2G (Addgene, 194457), which was digested with EcoRI and NotI, and the anti-mesothelin scFV from the Amatuximab sequence (PDB: 8CXC_A). The vector contains a GMCSF signal peptide, CD8A hinge transmembrane domain, and 4-1BB, and CD3 signaling domains as well as bicistronic expression of a dual GFP-Bleomycin selection cassette. The mesothelin scFV was cloned downstream of the GMSF signal peptide and in frame with the CD8A hinge to generate anti-mesothelin human CAR T-cells.

Subcutaneous tumors

NSG or C57/BL6J mice were shaved and ear tagged under isoflurane anesthesia. Cell suspensions (150,000 for NSG, 250,000 in C57BL6J) in a volume of 100 μl growth factor-reduced Matrigel (Corning, CLS356230) diluted 1:1 with PBS were implanted under the skin of left and/or right flanks using a 28-gauge syringe. The syringe was left under the skin for ten seconds to allow the Matrigel to solidify. For dye retention studies, $2x10^6$ mT4-2D cells expressing tdTomato-luc2-hCD19; p27k-mVenus were labelled with 5 μM of eFluor-660 cell proliferation dye (Invitrogen, 65084085) for ten minutes at 37°C, washed three times with DMEM, suspended in a 1:1 PBS: Matrigel solution, and injected subcutaneously in mice (250,000 cells/mouse).

Orthotopic pancreas tumors

Mice were prepped for surgery the day before by shaving and ear tagging. The day of surgery, mice received pre-operative analgesia (Ethiqa XR extended-release buprenorphine), administered by the University of Texas veterinary staff. Carprofen (MedVet International, 503045269) was diluted to a final concentration of 2 mg ml^{-1} in sterile saline and administered pre-operatively (10 mg kg^{-1}). Mice were anesthetized with 3% isoflurane and prepped for surgery by cleaning the abdomen with betadine solution and isopropanol three times each. Sterile eye lubricant (MedVet International, 730979) was applied before surgery. An initial 2 cm abdominal incision was made to expose the peritoneum, followed by a second 2 cm incision lateral to the spleen. The spleen and pancreas were extracted and placed on a sterile pre-wet cotton swab, and a 1:1 mixture of Matrigel:PBS (50μl) containing 50,000 mT2-2D or 200,000 KPC -/- cells was injected into the pancreas. The needle was held for 20 seconds to allow the Matrigel to solidify, and successful injections were verified by a small transparent bubble in the tail of the pancreas. The spleen and pancreas were carefully replaced, and the peritoneum was closed using 5-0 vicryl sutures (MedVet International, VCP593G) and outer skin with 9 mm wound clips (AutoClips, Braintree Scientific). Mice received post-operative analgesia using carprofen (10 mg kg^{-1}) every 24 hours for up to 72 hours post-surgery and were monitored two times per day for the initial 48-hour recovery period. Mice with extensive tumors outside of the pancreas but lacking pancreatic tumors (wound tumors from cell suspension spillover) were removed from the study.

For adoptive transfer of CAR T-cells, mice were placed on a doxycycline chow diet (Bio-Serv, 14-727-450) for three days prior to and 11 days after administration of CAR T-cells (For TetON-shRNA tumors). Mice received a single dose of cyclophosphamide I.P. (180 mg kg^{-1}), followed 24 hours later by an I.P. injection of 0.25 -5 million CAR T-cells. Tumors were collected three days post-CAR T-cell administration for spatial transcriptomics to limit the extent of cell death complicating the analysis. For other studies, tumors were harvested one week after CAR T-cell treatment; this time point was earlier than S.C. tumor studies to overcome the low and inadequate recovery of tumor cells for downstream analyses.

To deplete macrophages, the same adoptive transfer/doxycycline protocol was followed, except that clodronate liposomes (APExBio, K2721) or PBS-loaded vehicle control liposomes (APExBio, K2721) were additionally

injected I.P. on the day of and 72 hours after CAR T-cell administration. Each treatment consisted of 200 µl of vehicle or clodronate-loaded liposomes (5 mg ml^{-1}).

EREG neutralizing antibody production and purification

Neutralizing antibodies were produced by the Advanced Protein Therapeutics Core Facility at the University of Texas at Austin using clone H321 as the template [43]. VH and VL sequences were codon-optimized for CHO expression using the Twist Bioscience platform and synthesized with flanking regions for Gibson assembly into AbVec human IgG1 and human Igκ expression vectors. Constructs were assembled by Gibson cloning, transformed into DH5α cells, and selected on 2×YT agar containing 100 µg/mL carbenicillin.

For expression, anti-EREG VH (huIgG1) and VL (huIgK) plasmids were co-transfected into ExpiCHO cells (Thermo Fisher Scientific) following the manufacturer's High Titer protocol (7 days at 32°C, 5% CO_2). Clarified supernatants were diluted in Protein A binding buffer (25 mM Tris-HCl, 25 mM NaCl, pH 7.4) and purified using a HiTrap Protein A HP column (Cytiva) on an ÄKTA Pure FPLC system. Antibody was eluted with 100 mM sodium citrate, 100 mM NaCl (pH 3.0) and immediately neutralized with 1 M Tris (pH 8.0). Eluted fractions were pooled, concentrated, and buffer-exchanged into PBS using a 30 kDa MWCO centrifugal filter (Amicon Ultra-4).

To confirm EREG antibody binding, high-binding plates were coated overnight at 4°C with 2 µg/mL EREG-Fc (Sino Biological) in PBS. Wells were washed with PBS/0.05% Tween-20 (PBS-T) and blocked with PBS-T containing 5% non-fat milk for one hour at room temperature. Antibodies were added in duplicate starting at 5 µg/mL with serial 10-fold dilutions and incubated for one hour. After washing, goat anti-human κ-HRP (1:2000; Southern Biotech) was added for one hour. Plates were developed with TMB substrate, stopped with 1 M HCl, and read at 450 nm. Binding curves were fit using four-parameter logistic regression.

Animal imaging

For bioluminescence (BLI) imaging, mice were injected intraperitoneally with 100 µl of D-luciferin (Syd Labs, MB000102-R70170) dissolved in PBS (30 mg ml^{-1}). Animals were anesthetized with isoflurane for imaging using the IVIS instrument (Revvity) in the Biomedical Imaging Center (RRID:SCR_021898) within the Center for Biomedical Research Support at the University of Texas at Austin. Images were analyzed and quantified using the ROI function of the BLI signal in Living Image software v4.8.2 (IVIS imaging systems).

Murine T-cell culture and transduction

The day before spleen harvesting, 24-well dishes were incubated overnight at 4°C with 1 ml of PBS containing 5 µg ml^{-1} of anti-CD3 antibody (Biolegend, 100239). The following day, spleens were harvested from 6-8 week old C57/BL6 mice, minced with a razor blade, and forced through a 70 µM cell strainer. Single-cell splenocyte suspensions were treated with red blood lysis solution (eBioscience), neutralized with PBS, and re-suspended in 1 ml of mojo sort buffer (Biolegend) at a concentration of $1x10^8$ ml^{-1}. To generate sufficient numbers of CAR T-cells, spleens from two or three mice were pooled together. CD3+ T-cells were isolated using mojo sort CD3 mouse T-cell isolation kit (Biolegend) according to the manufacturer's instructions. T-cells ($1x10^6$ cells ml^{-1}) were active by culturing overnight in T-cell media (RPMI-1640 , 20% FBS, 50 µM B-ME, 1 mM sodium pyruvate (Corning), 1x non-essential amino acids (Cytivia), and 100 µg ml^{-1} Primocin) with 100 IU ml^{-1} recombinant murine IL-2 (R&D systems, 402ML) and 2 ug ml^{-1} anti-CD28 antibody (Biolegend, 102115) on the CD3 antibody-coated plates. The following day, 100x concentrated retrovirus was added to each well, and plates were covered with parafilm and spun for 90 minutes at 500g and 32°C. Cells were then incubated for two additional hours at 37°C and briefly spun down at 500g for three minutes at room temperature to remove virus. Fresh T-cell media containing 100 IU ml^{-1} IL2 was added, and cells were cultured for an additional 48 hours followed by the addition of 10 ng ml^{-1} recombinant human IL-7 (Cell signaling technologies, 50425) and IL-15

(Cell signaling technologies, 73786). Cells were cultured for up to 10 days, then directly used or cryopreserved. Transduction efficiency was assessed by GFP, mTagBFP2, or staining with an anti-G4S linker antibody, and flow cytometry. T-cells were resuspended in PBS and co-cultured with tumor cells or injected into mice I.P. at a dose of 1-5 x10^6 cells as described in the *Orthotopic pancreas tumors* section.

Generation of CAR retrovirus

All plasmids used to generate retrovirus or lentivirus were cloned and expanded in NEB Stable competent E. *coli* cells and isolated with a ZymoPURE II Plasmid midiprep kit (Zymo Research). HEK 293FT cells were seeded at 4 x10^6 ml^{-1} in 150 mm dishes coated with collagen I (Gibco) to prevent detachment. The following day, cells were transfected with 4 ug of pCl-Eco (Addgene, 12371) and 4 ug of anti-CD19 or anti-mesothelin CAR MSCV using Fugene HD (Promega). Specifically, plasmids were mixed with 400 μl Optimem (Gibco) and 24 μl Fugene and incubated for 20 minutes. Cells were transfected, and the media was replaced 24 hours later with 30 ml of DMEM containing 1% FBS and 25 mM HEPES (Corning). After 72 hours, media was collected, filtered through 0.45 μM syringe filters, and concentrated using a 4x precipitation solution containing of 40% PEG-8000 (Thermo Fisher) and 1.2 M NaCl (Thermo Fisher) in PBS. Precipitated virus was re-suspended in PBS at a 100x concentration, and media from three 150 mm dishes was pooled and concentrated to transduce 10^7 T-cells.

Stable cell line generation

HEK293FT cells were seeded on collagen I-coated 100 mm dishes at 4x10^6 cells per dish for 24 hours, then transfected with 2 μg of transfer plasmid along with the second-generation packaging plasmids: 1.5 μg psPax2 (Addgene, 12260) and 0.5 μg pMD2.G (Addgene, 12259) diluted in Optimem to a final volume of 40 μl. The Fugene HD reagent (12 μl) was mixed with 145 μl of Optimem for five minutes before adding plasmids and incubating for 15 minutes at room temperature. The DNA-Fugene mix was added to HEK293FT cells overnight, and the media replaced with DMEM containing 1% FBS, 25 mM HEPES, and 1% penicillin/streptomycin. Media was collected 48 and 72 hours post-transfection, pooled, passed through a 0.45 μM filter, and concentrated using 100K centrifugal units (Millipore Sigma, UFC9100) and centrifuging for 40 minutes at 1500g or a 4x PEG-8000-based concentration solution. For the PEG-8000 solution, 4-fold viral media was incubated 12-24 hours and centrifuged at 1,500g for 30 minutes. Pelleted virus was re-suspended 100X in PBS for 10 minutes at room temperature, followed by vigorous pipetting and centrifugation at maximum speed for one minute to pellet carryover debris. Viral supernatant was used immediately or stored at -80°C.

Cells were transduced for 24 hours and selected by FACS or antibiotics 48-72 hours post-transduction. Cells with multiple constructs were serially infected and selected by antibiotics or FACS with single constructs. For antibiotic selection, 5 μg ml^{-1} of puromycin (Invivogen) and blasticidin (Invivogen) was used.

Tumor digestion for FACS and flow cytometry

Subcutaneous and orthotopic tumors were harvested and placed in a culture dish containing DMEM containing 10% FBS and 1% penicillin/streptomycin on ice and minced with a razor blade. In some cases, a portion of the tumor was placed in 4% paraformaldehyde (PFA) prior to mincing. Minced tumors were collected in 5 ml of digestion media (DMEM containing 1% Penicillin/streptomycin, 0.125 mg ml^{-1} of collegnase IV (Stem Cell Technologies, 07909), 0.125 mg ml^{-1} Dispase (Stem Cell Technologies, 07913), and 10 μg ml^{-1} of DNAse I (Stem Cell Technologies, 07900)) and incubated for 1.5 hours at 37°C. Digested tumors were collected by centrifugation at 300g for 5 minutes and then re-suspended in 5ml of TryplE (Gibco) and 10 ug ml^{-1} DNase I for an additional 10 minutes at 37°C. Undigested tumor fragments were allowed to settle for one minute, and the supernatant was transferred to a new tube with excess PBS to neutralize TrypLE. Cells were filtered through 70 and 40 μM cell strainers to generate single-cell suspensions. Prior to FACS or flow cytometry cells were incubated with viability dyes diluted in PBS (zombie aqua (1:1000) (Biolegend, NC0476349), Ghost Red 710

(1:1000) (Cell Signaling Technology, 90232), or (1 μg ml^{-1} of 4', 6-diamidino-2-phenylindole, dihydrochloride (DAPI) (Cell signaling Technology, 4083)), washed, and then re-suspended in PBS with 1% FBS prior to FACS. FACS using BD Aria Fusion or SONY SH800 and flow cytometry using Cytek Aurora was performed at the Center for Biomedical Research Support Microscopy and Flow Cytometry Facility at UT Austin (RRID:SCR_021756)

Organoid formation

Organoids were generated by isolating and processing tumors as described in the *Tumor digestion for FACS and flow cytometry* section. Cells were re-suspended in PBS with 1% FBS and sorted based on negative or high mVenus expression in tdTomato+ cells. Cells were plated in 20 μl Matrigel domes at 1,000 cells per dome in pre-heated 24-well dishes. For orthotopic tumors, 100 cells were plated per well. Epcam $^{+}$ tumor cells were isolated using the mojosort mouse Epcam isolation kit (Biolegned), incubated with CD45-APC and DAPI for 20 minutes on ice, washed twice, and sorted in single cell mode (Sony MA900 sorter) directly into chilled 96-well dishes with non-solidified Matrigel (50μl per well-kept cold). Isolated tdTomato+ tumor cells were incubated at 37°C for ten minutes before adding media. Organoids containing ≥50 cells were counted 10 days after plating.

Limiting dilution analysis for tumor-initiating cell frequency

Tumors were isolated, digested, and subjected to FACS as described in the *Tumor digestion for FACS and flow cytometry* section. mVenus ^{negative} and mVenus ^{high} cells were mixed with PBS:Matrigel (1:1) and injected at 2-4 sites containing 1000, 500, or 100 cells in 100 μl. Tumor formation was assessed by palpation, and tumors were weighed two months after injection. For serial tumor formation, primary tumors were generated with 100 mVenus ^{High} cells and harvested two months later. Tumor cells were FACS sorted into mVenus ^{Negative} and mVenus ^{High} populations, and 500, 100, or 10 cells were injected into secondary recipients. Two months later, tumors were quantified and imaged. Tumor-initiating cell frequencies were calculated using the Extreme limiting dilution software [44].

***In vitro* 3D spheroid co-culture**

p27k-mVenus and tdTomato-luc2-hCD19 KPC cells were mixed with anti-hCD19 CAR T cells at effector-to-target (E:T) ratios of 0:1 (5,000 KPC cells only) or 5:1 (5,000 KPC cells:25,000 CAR T cells). Cell mixtures were pelleted at 300g for 5 minutes and resuspended in 100% growth factor–reduced Matrigel. Suspensions were plated as 10 μl domes in pre-warmed 24-well plates and allowed to solidify for 10 minutes at 37°C. Complete growth medium (DMEM with 10% FBS and 1× Primocin) containing 100 IU ml^{-1} IL-2 was added to each well. Cells were incubated for 48 h before analysis. For spheroid flow cytometry analysis, cells were recovered using TrypLE, stained with Zombie Aqua viability dye for 15 minutes on ice, and analyzed immediately.

***Ex Vivo* KPC: CAR T-cell co-culture**

p27k-mVenus and tdTomato-luc2-hCD19 cells (250,000) were implanted into NSG or C57/BL6 mice. After 10 days C57/BL6 mice received 5 million anti-hCD19 CAR T-cells, whereas NSG mice received no treatment. Two-weeks later, tumors from both NSG and C57/BL6 mice were isolated and digested into single-cell suspensions as described in the *Tumor digestion for FACS and flow cytometry* section. Viable, tdTomato+ cells were sorted from both NSG and C57/BL6 mice into 15 ml tubes containing DMEM with 10% FBS. mVenus ^{Negative} cells were isolated from NSG mice, and mVenus ^{High} cells from C57/BL6 mice. Cells were plated (500 cells/well) in 96-well plates. Three hours later, 5,000 CD3/28 activated CAR T-cells were added in media supplemented with 100 IU ml^{-1} of recombinant IL-2 and incubated for 48 hours. Cell viability was then quantified by luciferase activity by adding 100 μl of 50 μg ml^{-1} D-luciferin, incubating for 5 minutes, then recording luminescent signal (BioTek Synergy H1). All values were relative to tumor cells without CAR T-cells. Luc2 null cells and no-luciferin media conditions were used for background correction.

Ex Vivo Macrophage: CAR T cell conditioning

TAMs were isolated from three independent orthotopic tumors by mincing and digesting tissue for 45 minutes in 0.125 mg ml^{-1} collagenase, 0.125 mg ml^{-1} dispase, 10ug ml^{-1} DNAse, and 5% FBS. Tissues were passed through a 40 μM cell strainer and incubated with anti-F4/80-biotin antibody, followed by streptavidin enrichment using the mojosort mouse F4/80 selection kit according to manufacturer's instructions (Biolegend, 480170). $F4/80^+$ cells (25,000) were cultured on fibronectin (Corning, 354008) coated (10 μg ml^{-1}) coverslip-bottomed 24-well dishes (CellVis, P24-1.5H-N) for two hours to allow macrophage adherence before non-adherent cells were washed away with three PBS washes. Anti-mesothelin CAR T-cells were isolated by FACS five days after transduction using an Alexa-fluor 647 conjugated G4S linker specific antibody (Cell Signaling Technologies, 69782) and cultured with or without macrophages at a 1:3 CAR T:TAM ratio (8,333 CAR T-cells:25,000 TAMs per well) with or without 100 ng ml^{-1} recombinant EREG (rEREG) for 72 hours. All conditions were cultured in macrophage media (RPMI 1640 with 20% FBS, 2 mM L-glutamine, 2mM sodium pyruvate, 55 μM 2-mercapthoethanol, 10 ng ml^{-1} M-CSF, and Primocin (1X)). Media was supplemented with 10 ng ml^{-1} recombinant human IL-7 (Cell Signaling Technology, 73786) and IL-15 (Cell Signaling Technology, 50425) prior to the addition of CAR T-cells. After 72 hours, CAR T-cells were harvested and co-cultured with tdTomato-luciferease (Luc2) KPC target cells in a 96-well plate at a 1:1 (E:T) ratio for 48 hours. Luciferase activity was quantified as described in the *Ex Vivo KPC:CAR T-cell co-culture* section before the addition of CAR T-cells. After 24 hours, the CellEvent caspase-3/7 green detection reagent (Invitrogen, R37111) was added to each well according to the manufacturer's instructions and quantified using a plate reader (BioTek Synergy H1). IFNγ was quantified 48 hours after the addition of CAR T-cells by collecting 100 ul of media and assaying with an IFNγ Enzyme Linked Immuno-sorbent Assay (ELISA) (Biolegend, 430807). Cells were then washed three times with PBS, and the remaining viable KPC cells were quantified based on luciferase signal. Readings (relative luciferase units, RLU) were normalized to their respective pre-CAR T-cell values and expressed as fold changes to no T cell groups. Media-only controls were measured in parallel for background correction.

Flow cytometry

Tumors were digested as described in *Tumor digestion for FACS and flow cytometry* and cells were re-suspended in staining buffer containing 1% BSA. Cells were stained with antibodies for 15 minutes on ice, washed twice with PBS, and re-suspended in 400 μl of PBS for flow sorting. Single stain and unstained controls were used. For GFP^+ T-cells, fluorescent minus one controls (FMO) were used. All flow cytometry was performed on the Cytek Aurora and analyzed using FlowJo.

For intracellular antigens, cells were fixed in 4% PFA for 15 minutes, washed in PBS, and incubated on ice in 90% methanol for 10 minutes. Cells were then washed with PBS and incubated with antibodies for one hour followed by two more washes. For EREG staining, cells were also stained with anti-mouse Alexa fluor 647 secondary antibody for an additional 30 minutes. For CAR T-cell staining, whole blood was incubated with 1xRBC lysis buffer (ebioscience), washed twice, then stained and analyzed as above.

Western blotting

Cells were lysed with RIPA buffer (Thermo Scientific) for 5 min and scraped into 1.5 mL collection tubes and incubated on ice for 30 minutes. Lysates were centrifuged for 15 min at 15,000 rpm at 4°C, and protein concentration was measured using the Pierce BCA assay (Thermo Scientific). Lysates were diluted to 30 μg, resolubilized in 5x LDS loading buffer (Thermo Scientific), and heated to 95°C for 7 min. Samples were resolved on a 10% SDS-PAGE gel (Bio-Rad) and transferred to a nitrocellulose membrane using semi-wet transfer (Bio-Rad). Transferred membranes were blocked for 1 hour in 5% non-fat dairy milk (NFDM). Blocked membranes were washed with 1X Tris-buffered saline (TBS) + 0.1% tween-20 (TBST), then incubated with the diluted primary antibody overnight at 4°C. The following day, membranes were washed three times

with TBST followed by the addition of rabbit or mouse IgG secondary horse radish peroxidase (HRP) conjugated antibody diluted in 5% non-fat milk for 1 hour. Membranes were washed three times with TBST and developed using the West Super Femto substrate (Thermo Scientific).

RT-qPCR

Viable tdTomato^{+} mVenus ^{Negative} and mVenus ^{High} cells were sorted directly into Trizol (Invitrogen), and RNA isolated using the Zymo Direct-zol RNA micro or mini kit (Zymo Research). cDNA synthesis was carried out (100 ng of RNA) using the iscript cDNA synthesis kit (Bio-Rad). Undiluted cDNA (1 µl) was used for each PCR reaction using Power up SYBR green master mix (Thermo Scientific, A25741) according to the manufacturer's instructions. Gene expression was normalized to GAPDH and analyzed relative to mVenus ^{Negative} cells. Relative expression was calculated using the $2^{-\Delta\Delta CT}$ method, where $\Delta\Delta CT = \Delta CT\_sample - \text{mean } \Delta CT\_mVenus^{Neg}$.

Primers (5'-3'):

EREG:
Forward: CAGGCAGTTATCAGCACAACCG
Reverse: CATGCAAGCAGTAGCCGTCCAT
GAPDH:
Forward: CATCACTGCCACCCAGAAGACTG
Revers: ATGCCAGTGAGCTTCCCGTTCAG
NGF:
Forward: AGTTTTGGCCTGTGGTCGT
Reverse: GGACATTACGCTATGCACCTC
SPRR1A:
Forward: CAAGGCACCTGAGCCCTGCAA
Reverse: AGGCTCTGGTGCCTTAGGTTGG

Ultra-low input RNA-sequencing

Tumors from NSG mice with or without hCD19 expression were harvested two weeks after CAR T-cell therapy. Tumors were digested as described in *Tumor digestion for FACS and flow cytometry* but using RNAase-free DNase (Thermo Scientific). Samples were incubated with zombie aqua viability stain for 20 minutes, washed, and re-suspended in PBS with 1% FBS before FACS isolating mVenus ^{Negative} zombie aqua negative, tdTomato+ cells from hCD19^{-} tumors or viable mVenus ^{High} tumor cells from hCD19^{+} tumors. Cells were directly sorted into 300µl of Trizol and frozen at -80°C until ultra-low input RNA-seq was carried out by GeneWiz. Data were processed as previously described [45] with some alterations. Count matrices were normalized using Deseq2 and Log2Fold changes were filtered to absolute ± 5 and adjusted p-values <.01 between mVenus ^{Negative} and mVenus ^{High} cells to identify significantly altered genes. Gene names were copied from this data set and pasted into EnrinchR gene ontology for pathway analysis [46].

Human single-cell data analysis

Human patient data from obtained from gene expression omnibus GSE205013 was downloaded as a count matrix and processed using the Seurat package. Samples P04, P05, P07, P15, P19, and P23 were selected as they represented treatment-naive primary PDAC. Count matrices were uploaded to R studio and used to create a Seurat object. Cells expressing greater than 10% mitochondrial genes were filtered out. Data normalization and scaling, variable feature selection, and cell clustering were performed using the Seurat package in R. The data were normalized to total expression per cell and scaled by a factor of 10,000. The default Seurat "vst" method was used to select the top 2000 variable genes. These were subsequently subjected to principal component analysis (PCA) for dimensionality reduction. The first 30 principal components were selected using the elbow

method. 16 clusters were detected using the Louvain algorithm, which is the default Seurat method with a resolution set to 0.1. The resulting data was visualized using the Uniform Manifold Approximation and Projection (UMAP) algorithm. This data was then integrated, and a subset was generated based on Keratin 19 (KRT19) expression. This subset was then subjected to cell cycle analysis using the Seurat package, cell cycle score. The results were visualized using a dot plot to show the EREG, MKI67, and TOP2A features within the different cell cycle-based clusters.

Immunofluorescence of OCT-embedded and FFPE tissues

Tumors were harvested and placed in 4% Paraformaldehyde (PFA) for 30 minutes at room temperature. After 30 minutes, tissues were washed in PBS and a 30% sucrose solution overnight at 4°C. Tissues were embedded in OCT (Tisssue-Tek) and kept at -80°C until sectioning. For sectioning, 10 uM thick sections (Leica Cryostat) were cut onto slides pre-treated with Poly-L-lysine (Advanced Biomatrix, 5048) according to the manufacturer's instructions. Sections were dried for one hour, then kept at -20°C. Sections were brought to room temperature for two hours, then washed three times with PBS to remove OCT. Slides were blocked for one hour in blocking buffer (PBS with 5% FBS) and permeabilized for 20 minutes with 0.3% Triton-x-100 in PBS. For nuclear staining (Ki67 and mVenus reporter), slides were permeabilized with 1% Trixon-x-100 in PBS for one hour. Blocked slides were incubated with primary antibodies for 15 hours at 4°C in a modified humidity chamber, washed three times with PBS, and incubated with secondary antibodies for two hours at room temperature protected from light. After a second washing step, slides were mounted with DAPI-containing mounting media (Prolong Gold Antifade, Invitrogen). Slides were sealed with nail polish and allowed to dry overnight prior to imaging or subsequently stored at 4°C. Imaging was obtained within one week of slide prep. A Nikon A1R confocal microscope was used to acquire images, and ImageJ was used for quantification. To quantify the intensity of different regions of interest, single channels were used to first select cancer cells (RFP signal) using the ROI manager tool. This selection was overlayed onto GFP channel images (mVenus reporter) to identify reporter high and low regions using a threshold function. Fluorescent intensity of the EREG channel (Cy5) was measured within the regions of interest to obtain a % intensity/ROI. For whole-pancreas tumor images, slides were imaged with the upright Nikon Ni-E upright light microscope for large-image stitching. For whole pancreas image quantification, a threshold was set for each channel, and cells meeting the threshold were counted using Nikon Elements software. Only mVenus ^{High} cells (GFP/AF488) that surpassed the pan-cytokeratin (pan-cytokeratin/AF647) threshold were counted to prevent the inclusion of GFP+ CAR T-cells. Imaging was performed at the Center for Biomedical Research Support Microscopy and Flow Cytometry Facility at UT Austin (RRID:SCR_021756).

Processing, staining, imaging, and analysis of FFPE whole-slide tumors was carried out by iHisto (https://www.ihisto.io/). Sections (4 uM FFPE) from three independent tumors were mounted on a single slide and subjected to LiecaBond automated staining using tyramide signal amplification (TSA). Staining included: anti-ErBb4 (1:100) + rabbit-HRP + Cy5 TSA (1:100); anti-F4/80 (1:500) (provided by iHisto, cat #70076, clone: D2S9R) + rabbit-HRP + FITC TSA, and anti-EREG (1:25) + horse anti-mouse HRP + Texas Red TSA. Whole-slide scanning was performed using a 3DHISTECH Pannoramic MIDI II and quantified with HALO analysis software. Total ErBb4^{+} F4/80^{+} cells were quantified from the entire slide (n=3 tumors) based on EREG high and low regions of interest. iHisto also performed H&E staining and analysis by a board-certified DVM pathologist on three shEREG tumors isolated at day 150.

Human CAR T-cell culture and transduction

PBMCs were isolated from whole blood using a Ficoll-paque density gradient according to manufacturer's instructions (Millipore Sigma, GE17-1440-02). CD3 cells were then isolated from PBMCs using CD3 microbeads (Miltenyi, 130097043) and resuspended at 1x10^{6} per ml in T-cell media (Immunocult, Stem Cell Technologies) containing 100 IU ml^{-1} human recombinant IL-2 (Corning) and 2 μg ml^{-1} Ultra-LEAF purified anti-CD28 (Biolegend, 350902). Cells were plated on pre-coated plates (5 μg ml^{-1} anti-CD3 Ultra-LEAF purified anti-CD3, Biolegend, 300332) for 24 hours, then transduced overnight with anti-mesothelin CAR T-

cell lentivirus. Media was replaced after 24 hours, and two days later, cells were isolated by FACS based on GFP expression.

Human organoid co-culture

Low-passage PDX tumors (F3-F6) were minced and digested in 10 ml of DMEM containing 2% FBS, 1% penicillin/streptomycin, 0.125 mg ml^{-1} collagenase IV, 0.125 mg ml^{-1} Dispase II, and 10 μg ml^{-1} DNAse I and incubated for 45 minutes at 37°C. Digested tumors were further treated with TrypLE supplemented with 10 μg ml^{-1} of DNAse I for ten minutes at 37°C. Digested tumors were neutralized with DMEM and passed through 100 μM filters. To ensure that residual mouse stromal and immune cells were depleted, PDX-based organoids were passaged three times before experimentation. To obtain $CD14^+$ monocytes, PBMCs (obtained through We are Blood) were incubated with anti-CD14-FITC antibody (Miltenyi, 130113153) followed by anti-FITC beads (Miltenyi, 130097050) and magnetic selection using LS columns (Miltenyi) according to the manufacturer's instructions. $CD14^+$ cells and PDX tumor cells were mixed at 3:1 CD14: PDX (60K:20K) cell ratio and resuspended in a 1:1 mixture of Matrigel (4 mg ml^{-1}) and collagen I (3 mg ml^{-1}) pre-neutralized with sodium bicarbonate (7.5%) until the phenol red indicator in the Matrigel turned salmon pink. Domes (10 μl) were pipetted into the center of pre-warmed 24-well plates and allowed to solidify for 10 minutes at 37°C, followed by the addition of 500 μl of DMEM containing 15% FBS, L-glutamine, 0.01 mg ml^{-1}insulin, 0.01 mg ml^{-1} hydrocortisone, and Primocin. For the first two days of culture, 10 μM of a ROCK inhibitor (Y-27632, Millipore Sigma) was added to the media. After 72 hours of culture, 100,000 GFP^+ anti-mesothelin CAR T-cells were placed on top of the domes with PBS or 2.5μg ml^{-1} of EREG-neutralizing antibody. The media was supplemented with IL-7 and IL-15 (10 ng/ml) during this time. Matrigel domes were digested 48 hours later with TrypLE for 20 minutes. Cells were harvested, fixed, permeabilized, and stained for one hour using antibodies as described in the *Flow Cytometry* section.

Spatial Transcriptomics

Spatial transcriptomics was performed by the Genomic Sequencing and Analysis Facility at UT Austin, Center for Biomedical Research Support (RRID#: SCR_021713) using the Visium HD 3' Spatial Transcriptomics platform (10x Genomics) and the manufacturer's protocols (CG000803: Planner, CG000804: Tissue Prep (Rev A), CG000805: User guide (Rev A)). Tumors were collected and immediately placed in OCT molds on top of a dry ice/100% ethanol bath, then kept at -80°C. Tumors were sectioned at -20°C (thickness: 10 μm) and mounted on super frost gold slides (Fisherbrand). All surfaces were pretreated with RNAseZap (Thermo Fisher) prior to sectioning. Serial sections were also collected in 1.5 ml tubes to confirm RNA integrity through Qubit analysis (Thermo Fisher) prior to processing. Tissue sections were processed using the CytAssist Instrument (10x Genomics) to spatially barcode mRNA transcripts. Tissue sections were first fixed in chilled methanol and stained with Hematoxylin and Eosin (H&E) for histological visualization. Brightfield imaging was performed prior to permeabilization using a Nikon Ti2 microscope at 20x magnification using a plan apochromat λ 20x; NA - 0.75; WD - 1.0 mm objective. Images were later used for tissue alignment and annotation during downstream analysis. Following imaging, slides were loaded into the CytAssist instrument, which transferred spatial barcodes from the Visium HD slide to the tissue section, enabling capture of spatially resolved mRNA. After permeabilization, reverse transcription was carried out to synthesize cDNA with spatial barcodes. The resulting cDNA was amplified, and sequencing libraries were prepared according to the Visium HD 3' Gene Expression User Guide**.** Sequencing was performed on an Illumina NextSeq 1000 platform using paired-end reads at 240M reads. Raw data were processed using Space Ranger (V4.0) and aligned to the mouse reference genome (mm10).

Spatial Transcriptomic Analysis

Visium 3' HD data were processed using Scanpy v1.10 [47]**,** Squidpy v1.3 [48], and Python 3.10. Nuclear segmentation was conducted using Space Ranger v4.0.1 and the representative images were generated in Lupe Browser using the space ranger Lupe browser output file. T cells were identified by "CD8a"and "CD247",

EREG+ cancer cells by “EREG”,“MSLN”, and “KRT19”, and macrophages by “ITGAM” and “ADGRE1” in the 10x Genomics Lupe browser application (v9.0). At least 100 localized (segmented macrophages physically touching segmented EREG+ cancer cells) were manually selected for differential expression analysis vs. bulk tumor macrophages to assess EGFR and ERBB2-4 expression. For further analysis, 8 uM binned Space Ranger (v4.0.1) output files were used. Outputs were imported into AnnData [49], filtered to remove low-quality spots (<200 genes or <500 UMIs), and log-normalized to 10,000 transcripts per spot. Highly variable genes were selected using the Seurat-like method (3,000 highly variable genes (HVGs)), followed by scaling and principal component analysis (PCA) (50 components). Neighborhood graphs were constructed using 15 nearest neighbors, and embeddings were generated with uniform manifold approximation and projection (UMAP). Clustering was performed using the Leiden algorithm (resolution 0.8) [50]. Cell states were annotated using canonical marker genes from pancreas single-cell atlases [51] and by scoring lineage-specific signatures (epithelial, immune, endothelial, stromal) using Scanpy. Scores for macrophage, monocyte, T, B, NK, fibroblast, endothelial, acinar, ductal, and endocrine programs were computed using curated gene lists as follows: Macrophage: ["CD68", "CD163", "MRC1", "MARCO", "CSF1R", "ITGAM", "LYZ"], Monocyte: ["LY6C2", "LYZ", "S100A8", "S100A9", "VCAN", "IL1B"], Fibroblast: ["COL1A1", "COL1A2", "COL3A1", "FAP", "PDGFRA", "PDGFRB", "ACTA2", "TAGLN", "DCN", "LUM", "MMP2", "MMP11"], Endothelial: ["PECAM1", "VWF", "ESAM", "KDR", "ENG"], Pericytes: ["PDGFRB", "RGS5", "MCAM", "CSPG4"], Ductal: ["KRT19", "EPCAM", "MUC1", "KRT7", "SOX9"], Tumor: [“KRT19”, “EPCAM”, “MUC1”, “KRT8”, “KRT18”, “TACSTD2”, “SOX9”], Alpha:["GCG", "TTR", "IRX2"], Beta: ["INS", "IAPP", "PDX1"], T Cells: ["CD3D", "CD3E", "CD3G", "CD2", "TRAC", "IL7R", "CCR7"], NK Cells: ["NKG7", "GNLY", "GZMB", "PRF1", "KLRD1"], Dendritic Cells: ["ITGAX", "HLA-DPA1", "HLA-DPB1", "HLA-DRA", "HLA-DRB1", "CLEC9A", "IRF8"], Hypoxia Score: ["HIF1A", "CA9", "ENO1", "ALDOA", "LDHA"]. Spatial neighborhood and proximity analyses were performed on normalized log1p-transformed expression data using pixel coordinates. Tumor anchors were identified by epithelial markers (EPCAM, KRT19, MSLN) and EREG-high tumor anchors were defined as tumor/epithelial spots in the top 5% (95th percentile) of normalized EREG expression. Microenvironment cells were annotated by signature scoring (macrophage, fibroblast, lymphoid) and were considered localized to an EREG anchor when they lay within 50 pixels of any EREG+ anchor. For macrophage- and fibroblast-centric analyses, localized cells (within 50 pixels of EREG+ anchor) were subset and clustered using 2,000 HVGs, PCA (30 PCs), neighbors (n=10) and Leiden clustering (resolution=0.8) to delineate macrophage-like and fibroblast-like subclusters. Neighborhood composition around EREG-high and matched EREG-low anchors was computed by KD-Tree query [52] (radius = 50 pixels) and expressed as mean fractional composition per anchor; enrichment was calculated as the difference in mean fractions (High − Low) and standardized by z-score. Distance-to-anchor distributions were compared with Mann–Whitney U tests and proportions of localized cells with Fisher’s exact test; p-values were adjusted using Benjamini–Hochberg where applicable. Tumor cell EREG expression was quantified and Z-normalized. Spots were classified as EREG-high when above 1 standard deviation from the mean. Spatial neighbors were computed using Squidpy [48]. Heatmaps, UMAPs, and spatial feature plots were generated using Matplotlib [53], Scanpy, and Squidpy. Core packages included Scanpy 1.10, Squidpy 1.3, Anndata 0.10, NumPy 1.26, Pandas 2.1, and Matplotlib 3.8.

Results

Quiescent PDAC cells are enriched after CAR T-cell therapy

In order to identify and study quiescent PDAC cells, we engineered mT4-2D cells derived from a tumor formed in the KPC (Pdx1-Cre; $KRAS^{G12D/+}$, $p53^{R172H/+}$) mouse model [41] to express the live-cell quiescence reporter, p27k–mVenus. This reporter expresses the stabilized fusion fluorescent protein p27k-mVenus, which accumulates in quiescent cells and is degraded on cell-cycle entry [32] (Fig. 1a), and mVenus ^{High} cells were quiescent since they lacked the proliferation antigen Ki67 (Fig. 1b) and down-regulated cell-cycle transcriptional signatures (e.g., “G2–M checkpoint”, “E2F targets”) (Fig. 1c). Given that quiescent cancer cells can evade T cell recognition by down-regulating MHC class I [25-27], we also expressed human CD19 (hCD19) to serve as a defined target for CAR T-cells, as well as tdTomato and luciferase to track cells both *ex*

vivo and *in vivo* (Extended Data Fig. 1a). We initially studied subcutaneous tumors in NSG mice, which lack functional B, T, and NK cells, to limit anti-tumor immunity to CAR T-cells. Two weeks after treatment, anti-hCD19 CAR T-cells ($5x10^6$ cells) significantly decreased $hCD19^+$ tumors, whereas the growth of $hCD19^-$ and PBS-treated hCD19+ tumors was not impacted (Extended Data Fig. 1b,c).

We quantified quiescent cancer cells in residual tumors after CAR T-cell treatment, and the frequency of mVenus ^{High} cells was significantly higher in $hCD19^+$ tumors compared to tumors generated from $hCD19^-$ cells or PBS-treated animals (42% ± 5.5% vs ~6.4% in $hCD19^-$ with CAR T-cells, ~4% in $hCD19^-$ with PBS, and ~3% $hCD19^+$ with PBS; $p = 0.009$; Fig. 1d). We similarly found that mVenus ^{High} cells were enriched in subcutaneous tumors formed in immunocompetent C57BL/6 (BL6) mice by 2.4- and 5.2-fold after treatment with $1x10^6$ or $5x10^6$ CAR T-cells, respectively (Fig. 1e). Orthotopic tumors better recapitulate the PDAC TME and are more resistant to CAR-T cells than subcutaneous tumors [54], and CAR-T cell treatment increased mVenus ^{High} cells by 3.5-fold compared to PBS in this model (Fig. 1f). Therefore, quiescent cancer cells are enriched by CAR-T cells in subcutaneous and orthotopic PDAC models.

Cancer cells adopt a quiescent state post-therapy

Previous studies have demonstrated that long-lived quiescent cancer cells persist after immunotherapy [29, 33] or transiently arise from proliferating cells that adopt a quiescent phenotype [25, 26, 28, 55]. To determine the origin of PDAC quiescent cells in our models, we labelled mVenus ^{High} cells with the eFluor 660 proliferation dye prior to forming tumors in BL6 mice. Following CAR T-cell treatment, < 1% of the mVenus ^{High} cells were dye-retaining, suggesting these cells were not persistently quiescent (Extended Data Fig. 2a) [29, 33]. We also cultured mVenus ^{Negative} cells *in vitro* or formed tumors in NSG mice and found that mVenus ^{High} cells were generated in both conditions. Furthermore, tumors formed from mVenus ^{Negative} cells in BL6 mice and treated with CAR T-cells led to ~ 2.9x and ~1.5x higher frequencies of mVenus ^{High} cells than *in vitro* culture ($p = 0.001$) or NSG-derived tumors ($p = 0.025$), respectively (Extended Data Fig. 2b). This indicates that the quiescent state is plastic and acquired following exposure to anti-tumor immunity.

Quiescent cancer cells are not intrinsically resistant to CAR-T cells *in vitro*

To determine whether the quiescent phenotype is associated with resistance to adoptive immunotherapy, we compared *in vitro* CAR T-cell cytotoxicity of mVenus ^{High} cells isolated from CAR T-cell treated BL6 mice and mVenus ^{Negative} cells from untreated NSG mice. Tumor cells from NSG mice without CAR-T cell treatment were used as a comparator as they represent a relatively immune-sensitive cell population. Isolated cells were treated *in vitro* with CAR T-cells, and despite surviving therapy *in vivo*, mVenus ^{High} cells displayed no differences in sensitivity to CAR T-cell mediated killing compared to mVenus ^{Negative} cells from untreated tumors (Extended Data Fig. 3a-b). We also treated PDAC cells grown as spheroids in 3D cultures with or without CAR T-cells and found that treatment did not significantly impact the frequency of mVenus ^{High} cells (Extended data Fig. 3c). Therefore, quiescent PDAC cells are resistant to CAR T-cells *in vivo*, but not *in vitro*.

EREG is upregulated in quiescent cancer cells

The relative lack of intrinsic resistance to CAR-T cells *in vitro* suggests the enrichment of mVenus ^{High} cells *in vivo* is mediated by extrinsic mechanisms. RNA-seq studies identified several secreted factors highly expressed by mVenus ^{High} cells, which are involved in inflammation or immunity, including epiregulin (EREG), nerve growth factor (NGF), and small proline-rich protein 1a (SPRR1a) (Extended Data Fig. 4a). We knocked down each of these factors in PDAC cells, formed tumors in BL6 mice, and treated with CAR T-cells (Extended Data Fig. 4b-c). The loss of EREG, but not NGF or SPRR1a, significantly reduced the burden of quiescent cancer cells as quantified by p27k-miRFP670 expression compared to shRNA controls (Extended Data Fig. 4d-f). Notably, EREG knockdown did not impact quiescent cancer cells in the absence of CAR-T cell therapy (Extended Data Fig. 4e-f). We also confirmed that EREG expression was significantly higher in mVenus ^{High} cells than mVenus ^{Negative} cells isolated from tumors post-CAR-T cell therapy at the mRNA and protein levels

(Fig. 2a-b). To assess the clinical relevance of these findings, we examined a human PDAC single-cell RNA-seq dataset (GSE205013, n=6 treatment naïve patients) and found that EREG expression was increased in epithelial cells (Keratin 19, log2FC > 2.5) classified as G0/G1 (quiescent) compared to cycling cells expressing MKI67 (Ki67) and TOP2A (Fig. 2c). Furthermore, relatively high EREG expression is associated with significantly worse overall survival in human PDAC, with a 5-year survival rate of 0% in EREG-high patients compared with 33% in EREG-low patients ($p < 0.0001$; Fig 3a). Thus, EREG is selectively upregulated in quiescent cancer cells *in vivo*.

Tumor-derived EREG impacts CAR-T cell activity *in vivo*

EREG has been identified as part of a five-gene prognostic signature (MET, ERAP2, IL20RB, EREG, and SHC2) in human PDAC, associated with reduced $CD8^+$ T-cell infiltration and increased T-cell dysfunction [39]. Furthermore, we found that relatively high EREG expression is associated with significantly worse overall survival in human PDAC, with a 5-year survival rate of 0% in EREG-high patients compared with 33% in EREG-low patients ($p < 0.0001$; Fig 3a), implicating EREG as a potential regulator of anti-tumor immunity and a determinant of clinical outcome in PDAC.

To determine whether EREG modulates CAR T-cell activity *in vivo*, we knocked down its expression in cancer cells using doxycycline-inducible EREG shRNA. While our initial studies used hCD19 as a model target antigen, we studied anti-mesothelin CAR T-cells, which are currently under clinical testing for advanced PDAC [4]. Notably, EREG knockdown did not impact orthotopic tumor growth in NSG mice or sensitivity to anti–mouse mesothelin CAR-T cells *in vitro* (Extended Data Fig. 5a,c,e,f), indicating that EREG does not directly regulate tumor cell growth or intrinsic CAR T-cell resistance.

Mice with inducible EREG (shEREG) or a scramble control (shScramble) shRNA were administered doxycycline starting three days prior to anti-mesothelin CAR T cells (5e6) and continued for a total of 14 days. Compared to both untreated controls (shScramble + PBS) and CAR T-cell–treated controls (shScramble + CAR T), EREG knockdown in cancer cells significantly increased median survival from 36–38 days to 136 days ($p < 0.0009$; Fig. 3b). Notably, EREG knockdown resulted in complete tumor eradication in 50% of treated mice (3/6), with histological analysis confirming the absence of microscopic disease in pancreatic tissues at day 150 (Fig. 3c). Consistent with its role as a predictor of T-cell dysfunction and infiltration in human PDAC, EREG knockdown significantly increased overall $CD3^+$ T-cell infiltration, including the frequency of $IFN\gamma^+$ $TNF\alpha^+$ CAR T-cells (GFP^+ $CD8^+$) and Granzyme B $(GZMB)^+$ $CD3^+$ T-cells compared with control tumors (Fig. 3d–f). Together, these results demonstrate that EREG expression in PDAC cells shapes both the distribution and functional activity of CAR T-cells.

EREG loss enhances quiescent cell targeting by CAR T-cells

Given the elevation of EREG expression in quiescent cancer cells following CAR T-cell therapy, we next tested whether EREG knockdown enhances the sensitivity of these otherwise (*in vivo*) immune-resistant cells. Compared with control (shControl) tumors, EREG knockdown (shEREG) tumors exhibited significantly reduced frequencies of mVenus ^{High} cells after CAR T-cell treatment, an effect not observed with PBS treatment (Fig. 4a–b). Furthermore, a higher proportion of mVenus ^{High} cells from shEREG tumors were apoptotic and expressed cleaved caspase-3 ($CC3^+$) (Fig. 4c) post-therapy, indicating that their reduction is due to increased killing rather than impaired entry into quiescence. Consistent with enhanced CAR T-cell mediated killing, shEREG tumors contained higher numbers of $CD3^+$ T-cells in direct contact with mVenus ^{High} cells compared to shControl tumors (Fig. 4d). We examined a second PDAC model, KPC -/- ($p53^{-/-}$), which harbors a null TP53 allele distinct from the dominant-negative $TP53^{R172H/+}$ mutation present in mT4-2D cells, and EREG knockdown similarly reduced the frequency of mVenus ^{High} cells and increased their apoptosis compared with shControl tumors (Extended Data Fig. 6a–c).

To validate these findings in human PDAC, we established a 3D co-culture model using mesothelin-expressing PDX-derived tumor cells. The PDAC tumor microenvironment is characterized by dense fibrosis and extensive immune infiltration, with tumor-associated macrophages representing the dominant population [7]. As such, we co-cultured PDAC tumor cells with $CD14^{+}$-derived macrophages and embedded them in collagen I to recapitulate the native TME (Fig. 4e, Extended Data Fig. 7a). Treatment with anti-mesothelin CAR T cells and an EREG-neutralizing antibody (EREG NAb; Extended Data Fig. 7b) significantly increased the frequency quiescent cancer cells ($EpCAM^{+}$ $CC3^{+}$ $p27^{High}$) compared to CAR T-cells alone (Fig. 4f). Consistent with our EREG knockdown murine models, EREG neutralization had no effect when tumor cells were cultured directly with CAR T-cells, indicating that EREG does not mediate intrinsic resistance to CAR T-cell cytotoxicity (Extended Data Fig. 7c). Collectively, these data demonstrate that EREG indirectly protects quiescent cancer cells from CAR T-cell–mediated killing.

Quiescent cancer cells exhibit stem-like, tumor-propagating properties

Quiescent cancer cells have been implicated in tumor regrowth and disease relapse following treatment [18, 56], and we found that mVenus ^{High} cells expressed higher levels of transcripts associated with CSCs compared to mVenus ^{Negative} cells, including PROM1 (CD133), ALDH1A3, F3, and AQP5 (Fig. 5a) [18, 57]. Functionally, mVenus ^{High} cells exhibited increased organoid formation *in vitro* and tumor-initiating cell frequency *in vivo*, produced larger tumors, and enhanced self-renewal during serial transplantation (Figs. 5b-e). We also found that cells isolated from shEREG tumors treated with CAR T-cells formed significantly fewer organoids compared to shControl tumors (Extended Data Fig. 8a-b). In contrast, EREG knockdown *in vitro* did not affect organoid-forming capacity, even with continuous doxycycline exposure for ten days prior to analysis (Extended Data Fig. 8c). Together, these results suggest that quiescent tumor cells possess functional stem-like properties and EREG does not directly affect these properties but rather promotes their resistance to CAR-T cells *in vivo*.

We also studied the role of EREG in tumor recurrence following treatment by treating mice with $2.5x10^6$ CAR T-cells. We utilized this lower CAR T-cell dose since we found that $5x10^6$ cells completely eradicated tumors in 50% of mice (Fig. 3b-c). While 67% of the shControl tumor-bearing mice relapsed by 40 days after treatment, 100% of the mice with shEREG tumors remained relapse-free at day 60 (Extended Data Fig. 8 d-e). Together, these findings indicate that EREG knockdown delays tumor recurrence, potentially through CAR T-cell targeting of the CSC pool.

ErBb4 expressing tumor associated macrophages are spatially localized to EREG.

To better understand the mechanism by which EREG impacts the TME, we performed spatial transcriptomic profiling of orthotopic tumors three days after CAR-T cell therapy (Fig. 6a). Tumor regions with high EREG expression (EREG ^{High}), defined as the top 5% of normalized EREG expression in tumor cells, were enriched for macrophages, monocytes, and fibroblasts (Fig. 6a-b). Re-clustering of cells within these EREG ^{High} regions revealed preferential enrichment of macrophage gene signatures relative to fibroblasts (Extended Data Fig. 9a). We also found that macrophages proximal to $EREG^{+}$ tumor cells (localized tumor-associated macrophages, TAMs) expressed the EREG receptor *ErbB4* at 4.5-fold higher levels than bulk macrophages, whereas the expression of *EGFR* and other *ErbB* family members was not significantly altered (Fig. 6c). We confirmed these finding by immunostaining and found increased $ErbB4^{+}$ $F4/80^{+}$ macrophages within EREG ^{High} tumor regions, in contrast to EREG ^{Low} regions, which consisted of $F4/80^{+}$ macrophages lacking ErbB4 expression (Fig. 6d). Localized induction of ErbB4 by macrophages can be induced by EGF-family ligands, such as Neuregulin-4 [58], suggesting that EREG itself may drive ErbB4. We quantified ErbB4+ macrophages (F4/80) by flow cytometry and found that tumors with EREG knockdown had a significantly lower frequency of $ErbB4^{+}$ $F4/80^{+}$ macrophages than control tumors in both the mT4-2D and KPC -/- models (Fig. 6e and Extended Data Fig. 9b).

EREG promotes CAR T-cell immune suppression through tumor-associated macrophages

To determine whether macrophages are required for EREG-mediated immune suppression, we depleted macrophages *in vivo* using clodronate liposomes (Fig. 6f). Consistent with prior results, shEREG tumors treated with control PBS-liposomes showed a significant reduction in mVenus ^{High} cells following CAR T-cell therapy (Fig. 6g). This effect was abolished by macrophage depletion, with no difference in mVenus ^{High} cell frequency observed between shControl and shEREG tumors (Fig. 6g).

To further define this mechanism, anti-mesothelin CAR T cells were cultured *in vitro* with or without tumor-associated macrophages (TAMs) and/or recombinant EREG (rEREG; Extended Data Fig. 9c). Exposure of CAR T-cells to rEREG did not alter intrinsic cytotoxic function or phenotype, as assessed by tumor cell killing, caspase-3/7 activation, and IFNγ secretion (Extended Data Fig. 9d–f). By contrast, rEREG significantly potentiated TAM-mediated suppression of CAR T-cell cytotoxicity and IFNγ production (Extended Data Fig. 9d–f). Collectively, these findings indicate that EREG impairs CAR T-cell function indirectly via TAMs rather than through direct effects on CAR T cells.

Discussion

The PDAC TME limits the activity of immune-based therapies, and we found that quiescent cancer cells promote immunosuppression following treatment with CAR T-cells. Quiescent cells, including those with CSC characteristics, actively remodel the pre-existing TME to establish immune-suppressive barriers [33, 59, 60]. Here, we demonstrate that quiescent PDAC cells drive further immunosuppression in an ErbB4^{+} macrophage-dependent manner, and the loss of EREG in cancer cells sensitizes tumors to CAR T-cell therapy. EREG inhibition also increased quiescent CSC killing, limited tumor regrowth, and improved survival.

Under physiological conditions, EREG is low or absent in most adult tissues but can be induced during inflammation and tissue regeneration [34-36, 61, 62] via NF-κB and IL-1β signaling [61, 63]. In colitis models, EGFR and ErbB4 drive the polarization of anti-inflammatory macrophages to limit tissue damage [58, 64]. In our study, EREG-expressing quiescent cancer cells co-localized with ErbB4^{+} TAMs following CAR T-cell therapy, while EREG conditioned macrophages displayed enhanced immune suppressive properties. These findings raise the possibility that CAR T-cell–induced inflammatory signals may trigger EREG expression, which in turn drives ErbB4^{+} TAM–mediated immunosuppression. Future studies will be necessary to fully elucidate the mechanism behind EREG induction in quiescent cancer cells.

EREG silencing sensitized both bulk and quiescent cancer cell populations to CAR T-cell therapy and significantly extended survival and delayed relapse. In addition, EREG neutralization enhanced CAR T-cell–mediated killing of quiescent cancer cells in human PDAC models. These findings suggest quiescent cancer cells not only promote immunosuppression in the TME but also represent a key reservoir of clonogenic cells driving tumor regrowth and recurrence. Together, these data establish EREG as a functional determinant of CAR T-cell efficacy and a candidate target for combinatorial immunotherapy strategies. Clinical studies examining EREG inhibition are limited, but the dual EREG/TGFα-neutralizing antibody LY3016859 has been studied in patients with diabetic nephropathy and is well tolerated [65]. Therefore, the rational combination of EREG blockade with anti-mesothelin CAR T-cell therapy, which is currently being evaluated in clinical trials for PDAC, may be feasible [4].

Our results position quiescent cancer cells to possess active TME-modifying effects through EREG secretion in PDAC. By inducing an EREG–ErbB4 signaling axis within the tumor microenvironment, quiescent cancer stem-like cells orchestrate macrophage-mediated suppression of CAR T-cell activity. Thus, this current work provides a mechanistic rationale for combining CAR T-cell therapy with EREG blockade to promote durable treatment responses.

Author contributions

BM designed and performed all experiments and wrote the manuscript. QW assisted with cell culture and *in*

vitro experiments. KA provided clinical expertise, experimental guidance, and manuscript editing. WM provided experimental guidance, secured funding, and edited the manuscript. All authors reviewed and edited the manuscript.

Acknowledgements

We thank all members of the Matsui laboratory for their support, with special acknowledgment of Shivani Malpotra and Qiuju Wang. This work would not have been possible without the exceptional assistance of the University of Texas veterinary staff and animal technicians. We are grateful to the blood donors who provided peripheral blood mononuclear cells through We Are Blood, as well as to the patients who generously donated tissues. We also thank the Dell Medical School nursing and clinical staff for their assistance with tissue transport and handling. We acknowledge Annalee Nguyen of the Advanced Protein Therapeutics Laboratory for generating the EREG-neutralizing antibody. Additionally, we thank the University of Texas core facilities, including the Flow Cytometry and Imaging Core, the Genomic Sequencing and Analysis Core, and the Biomedical Imaging Core. Finally, we appreciate iHisto and GeneWiz for their contributions to tissue processing, imaging, analysis, and sequencing.

Competing Interest

The authors declare no competing interest.

Data code and availability

Bulk RNA-seq (GSE 311363) and spatial transcriptomic (GSE 311362) data have been deposited to gene expression omnibus (GEO). RNA-seq data was analyzed using Deseq2 in R studio [66]. scRNA-seq data (GSE205013) was downloaded from GEO and processed using the Cell Ranger pipeline. Spatial transcriptomics was processed using spaceranger and the outputs were further analyzed by using squidpy and lupe browser [48]. All programming was carried out using the specified packages. No code was produced. We will gladly provide any other data upon request.

p27k-mVenus reporter validation

a

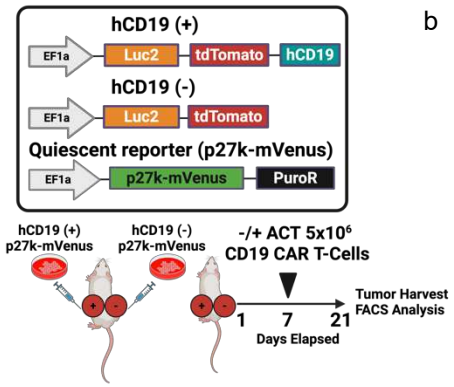

b

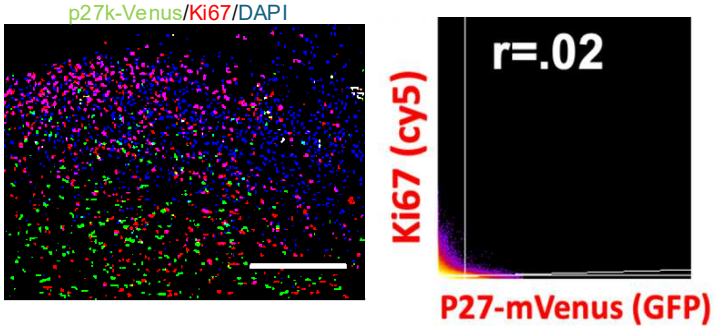

p27k-mVenus reporter validation

Quantifying p27k-mVenus high cells two-weeks post PBS or ACT (subcutaneous)

c

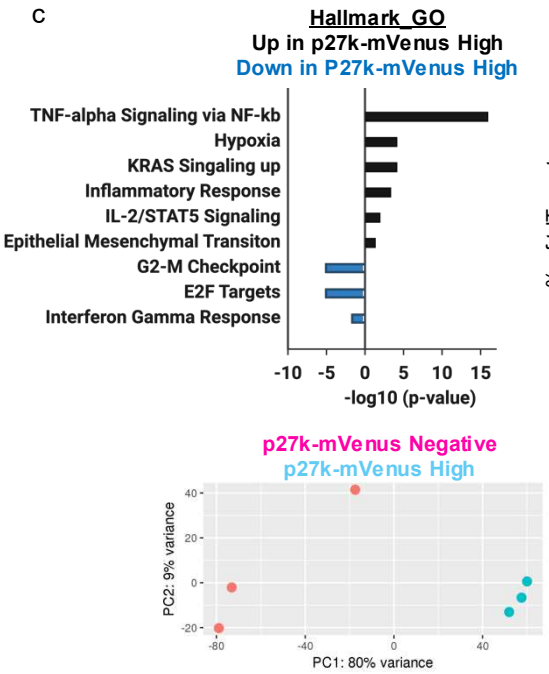

d Viable tdTomato⁺ mVenus ^{High}

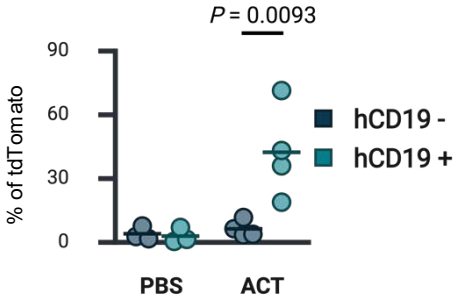

e Viable tdTomato⁺ mVenus ^{High}

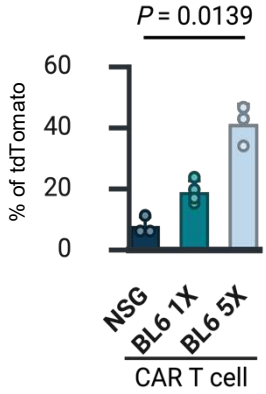

Orthotopic tumors post 1-week PBS or ACT

f

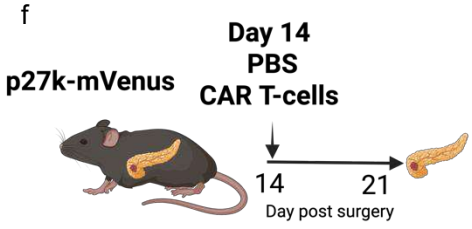

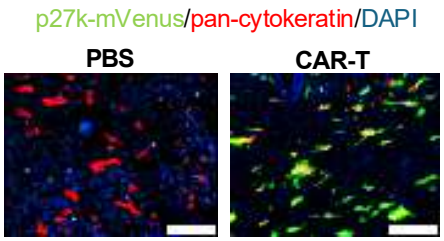

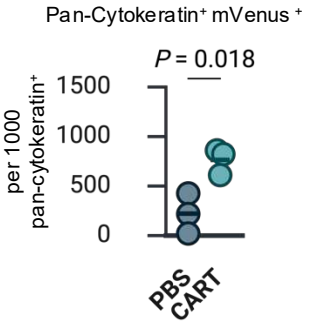

Figure 1. Quiescent PDAC cells are enriched post-CAR T-cell therapy. a, Experimental design schematic illustrating tumor implantation, treatment, and downstream analyses. **b**, Immunofluorescence of p27k-mVenus (anti-GFP, Alexa Fluor 488) and Ki67 (Alexa Fluor 647) in tumor sections. Co-localization of mVenus ^{High} and Ki67 was quantified using the Pearson correlation coefficient. **c**, Principal component analysis (PCA) of RNA-seq samples from mVenus ^{Negative} and mVenus ^{High} tumor cells (n = 3 per group) with gene ontology analysis of transcripts up- or down-regulated in mVenus ^{High} cells. **d**, Percentage of mVenus ^{High} cells within (Zombie Aqua ^{Neg}) viable, tdTomato^{+} tumor cells (n = 3–4 tumors per group). Statistical significance was assessed by two-way ANOVA with Tukey's multiple-comparison test. **e**, Quantification of tdTomato^{+} mVenus ^{High} cells in NSG (n = 3), BL6 1× (n = 4), and BL6 5× (n = 3) tumors. Statistical significance was determined using the Kruskal–Wallis test with Dunn's multiple-comparison test. **f**, Immunofluorescence of orthotopic pancreatic tumors one week after PBS or CAR T-cell treatment. Dot plots show mVenus ^{High} (GFP/Alexa Fluor 488) cells per 1,000 pan-cytokeratin^{+} cells (Alexa Fluor 647) (mean ± s.d., n = 3 tumors per group; unpaired two-tailed t-test). RNA-seq data from panel **c** were also used in Fig. 5a and Extended Data Fig. 4a. All figures and illustrations were created in https://BioRender.com.

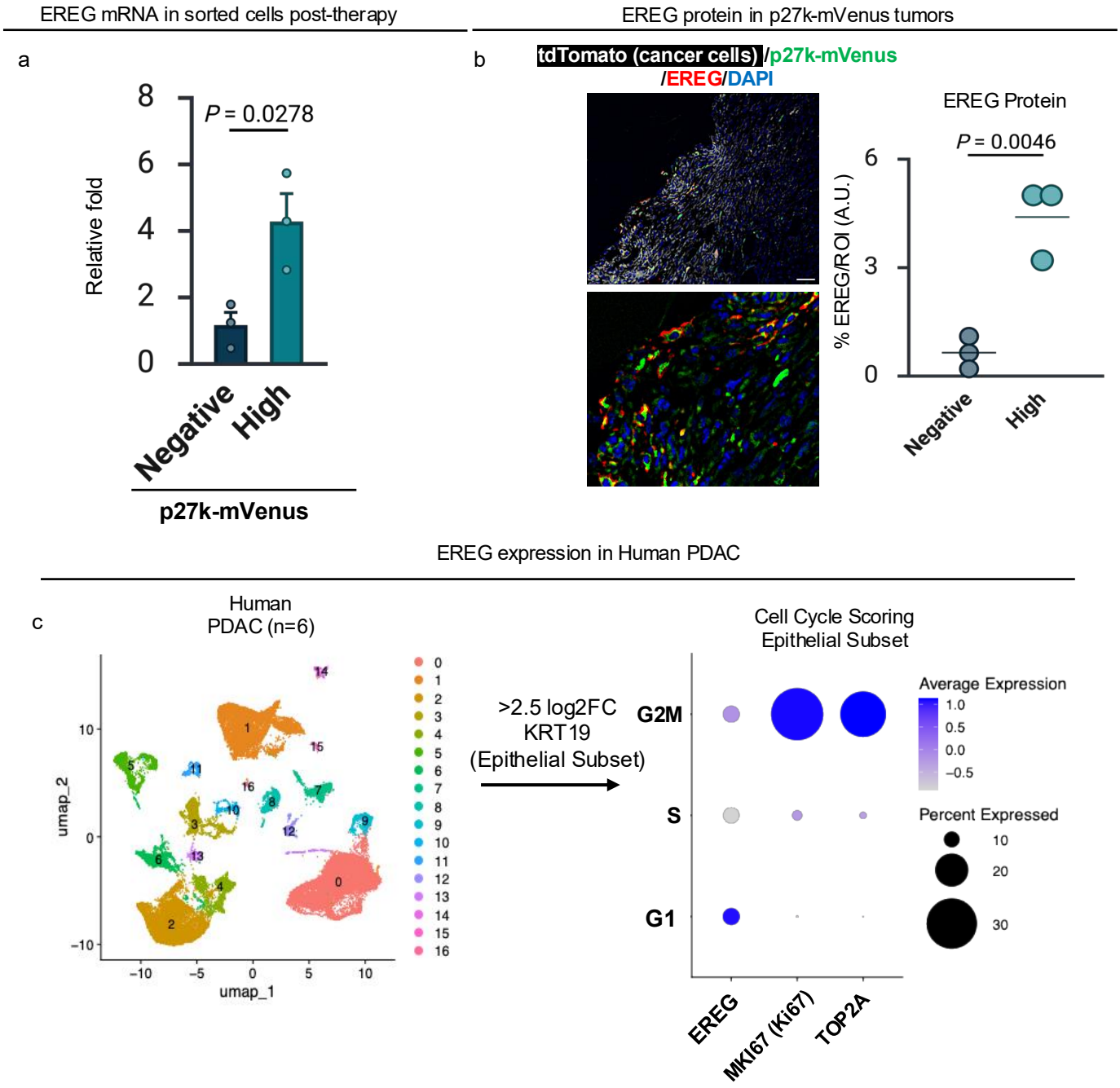

Figure 2. EREG is upregulated in quiescent cancer cells. a, RT–qPCR analysis of *EREG* mRNA mVenus ^{Negative} and mVenus ^{High} tdTomato^{+} tumor cells isolated by FACS from tumors formed in BL6 mice and treated with CAR T-cells (BL6 + ACT). Transcript levels were normalized to GAPDH and expressed as fold change relative to the mean of mVenus ^{Negative} cells (n = 3 independent tumors). **b**, Representative immunofluorescence

of tumor sections from BL6 mice post CAR T-cell therapy. EREG (Alexa Fluor 647) intensity was measured in tdTomato^{+} (mCherry/Alexa Fluor 555) mVenus ^{Negative} or mVenus ^{High} (GFP/Alexa Fluor 488) regions of interest (ROI). Each point represents the percentage of EREG intensity in tdTomato^{+}, mVenus ^{Negative} ROIs relative to tdTomato^{+}, mVenus ^{High} ROIs from the same tumor. DAPI was used for nuclear counterstaining. Three to four regions per tumor were analyzed and averaged together per tumor count (n = 3; unpaired two-tailed t-test). **c**, Analysis of *EREG* expression across distinct cycling states in epithelial (KRT19^{+}, $\log_2$FC > 2.5) cells from primary PDAC patient samples (n = 6). Cell-cycle stratification was validated using *MKI67* and *TOP2A* transcripts. All figures were created in https://BioRender.com.

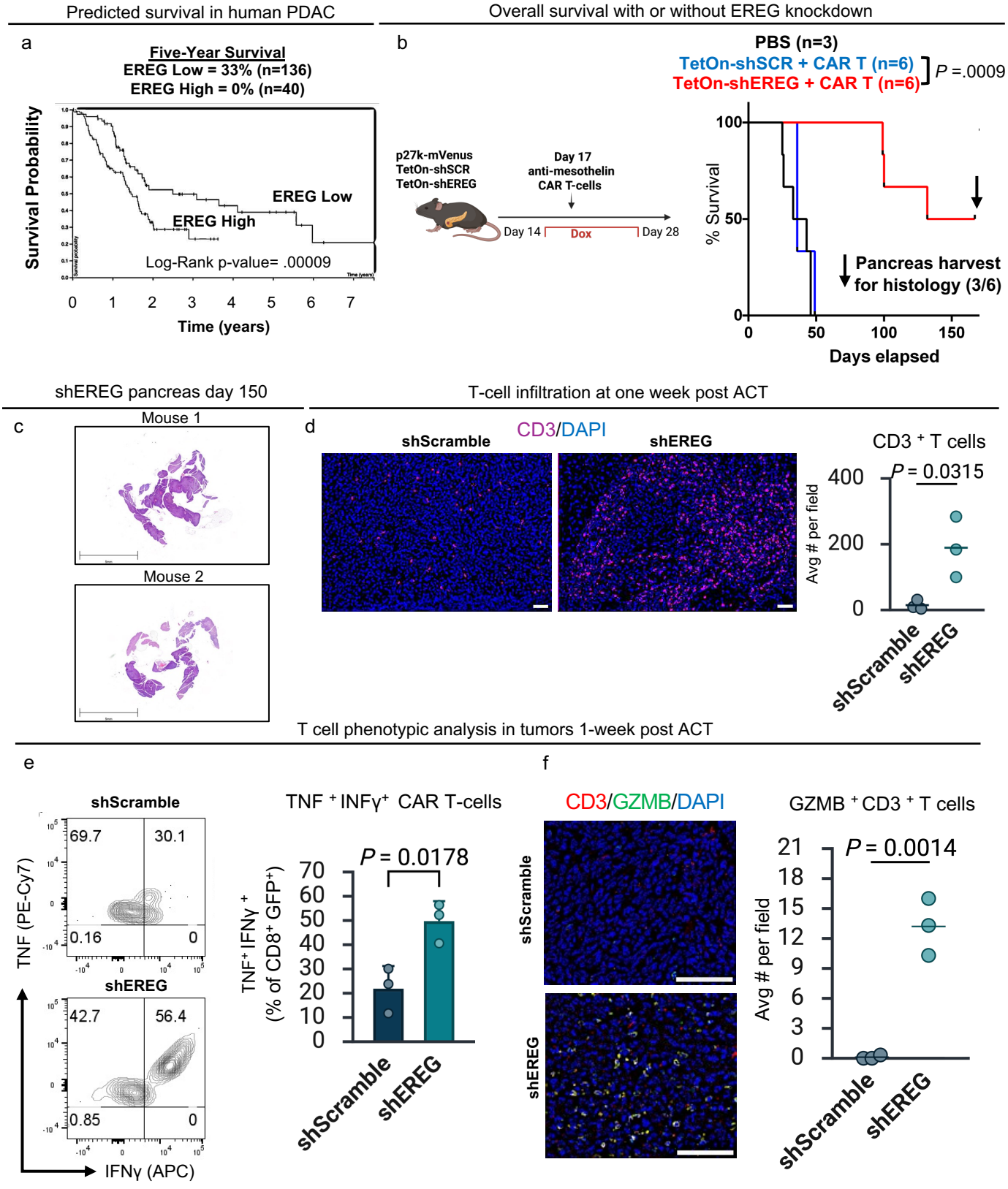

Figure 3. Tumor-derived EREG impacts CAR-T cell activity *in vivo*. a, Kaplan–Meier survival of PDAC patients stratified by *EREG* mRNA using a pTPM cutoff of 4.43. Patients were grouped into high (*EREG* > 4.43, $n = 40$) and low (*EREG* < 4.43, $n = 136$) cohorts. Significance was determined by two-sided log-rank test. **b**, Kaplan–Meier curves of mice bearing orthotopic TetOn-shScramble tumors treated with PBS ($n = 3$), TetOn-

shScramble tumors with CAR T-cells (n = 6), or TetOn-shEREG tumors with CAR T-cells (n = 6). Significance was assessed using two-sided log-rank test. **c**, Representative H&E staining of TetOn-shEREG tumors at day 150 post-implantation (n = 3). Histopathology to confirm absence of disease was performed by a board-certified DVM in anatomic pathology. **d**, Quantification of $CD3^+$ T cells in tumors one week post adoptive transfer. CD3 (Alexa Fluor 700) was measured using FIJI 3D Cell Counter. Data represent mean per tumor (n = 3; unpaired two-tailed t-test). **e**, Tumor-infiltrating CAR T cells ($CD8^+GFP^+$) analyzed for IFNγ and TNFα one week after transfer. Data are mean ± s.d. (n = 3 tumors, unpaired two-tailed t-test). **f**, Immunofluorescence of tumors one week post CAR T therapy stained for CD3, granzyme B (GZMB), and DAPI. Three tumors per condition were analyzed with ≥ 3 regions per tumor. Dot plots show mean $CD3^+GZMB^+$ cells per tumor (n = 3; unpaired two-tailed t-test). The same stained tissues from Fig. 3d were used for analysis in Fig. 4d by including mVenus (GFP) stained cells. Figures c–f were created in https://BioRender.com.

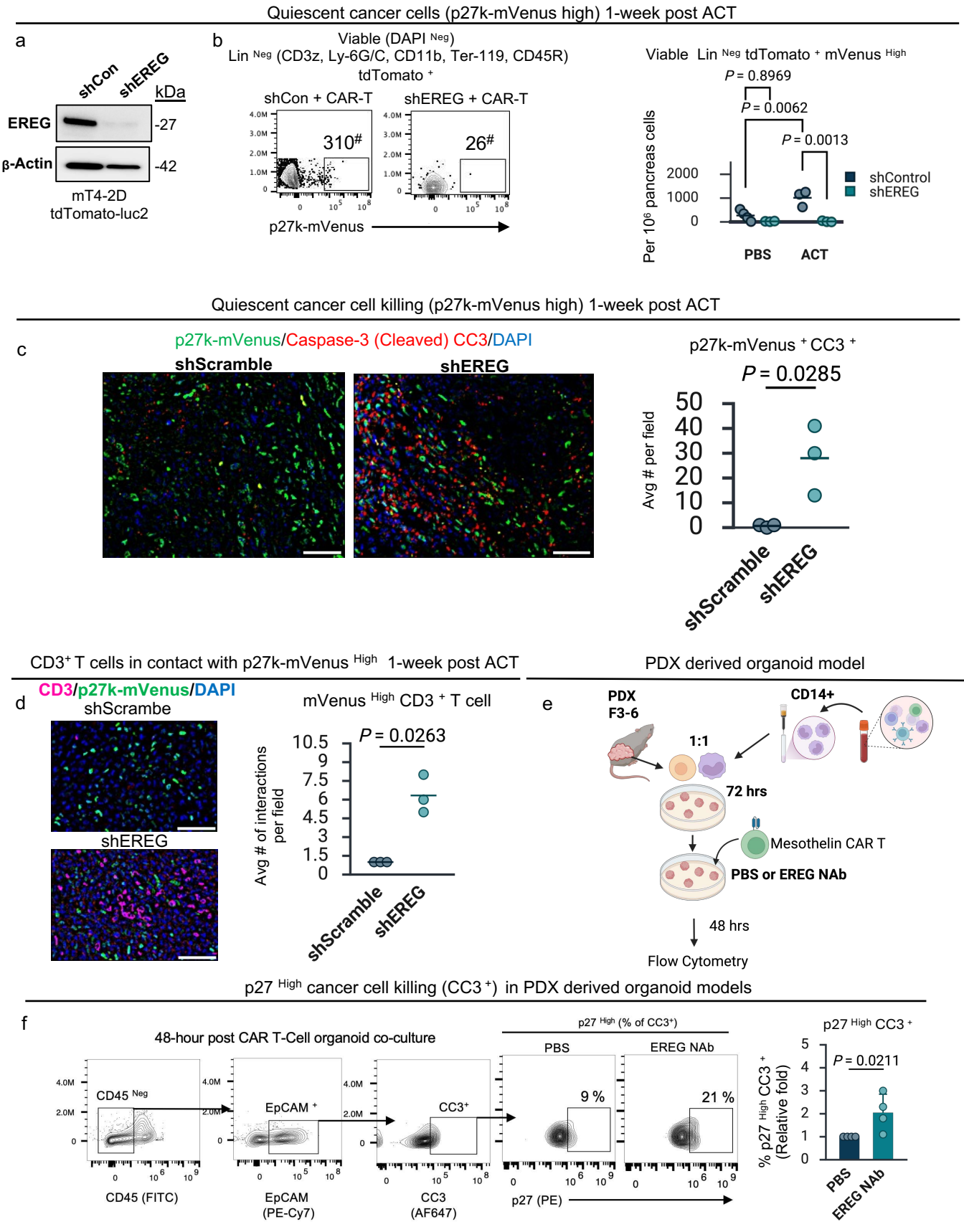

Figure 4. EREG protects quiescent cancer cells during CAR T-cell therapy. a, Western blot showing EREG knockdown (shEREG) versus control (shCon) tumor cells. Uncropped blots are in the Supplementary Information. **b**, Flow cytometry of orthotopic pancreatic tumors one week after PBS or 5 × 10^6 anti-mesothelin CAR T-cells. Contour plots show mVenus ^{High} cells within viable ($DAPI^-$), lineage-negative, $tdTomato^+$ cells.

Graphs quantify mVenus ^{High} cells per 10^6 viable cells ($^{\#}$ denotes cell number vs percentage), comparing shControl and shEREG tumors ($n = 3$ per group, two-way ANOVA with Bonferroni's multiple comparisons test). **c**, Immunofluorescence of inducible shScramble and shEREG tumors one week after CAR T-cell therapy using mVenus (GFP/Alexa Fluor 488) and cleaved caspase-3 (CC3; Alexa Fluor 647), with DAPI. Graph shows the mean mVenus$^+$ and CC3$^+$ cells from 2–3 fields per section across three tumors ($n = 3$; unpaired two-tailed *t*-test). **d**, Immunofluorescence of tumors stained for CD3 (Alexa Fluor 700) and mVenus (GFP/Alexa Fluor 488). Dot plots show mean CD3–mVenus$^+$ interactions per field (3 fields per tumor; $n = 3$; unpaired two-tailed *t*-test). **e**, Schematic of PDX-derived organoid co-culture. CD14$^+$ monocytes were co-cultured with PDX-derived tumor cells and CAR T cells ± EREG neutralizing antibody (EREG NAb). **f**, Flow cytometry of quiescent cancer cells 48 h post CAR T-cell addition ± EREG NAb. Contour plots show apoptotic (CC3$^+$), p27 ^{High} cells. Bar graph shows % CC3$^+$ p27 ^{High} cells from four independent organoid models ($n = 4$; mean ± s.d.; two-tailed Mann–Whitney U test). All figures, except contour plots, were created in https://BioRender.com.

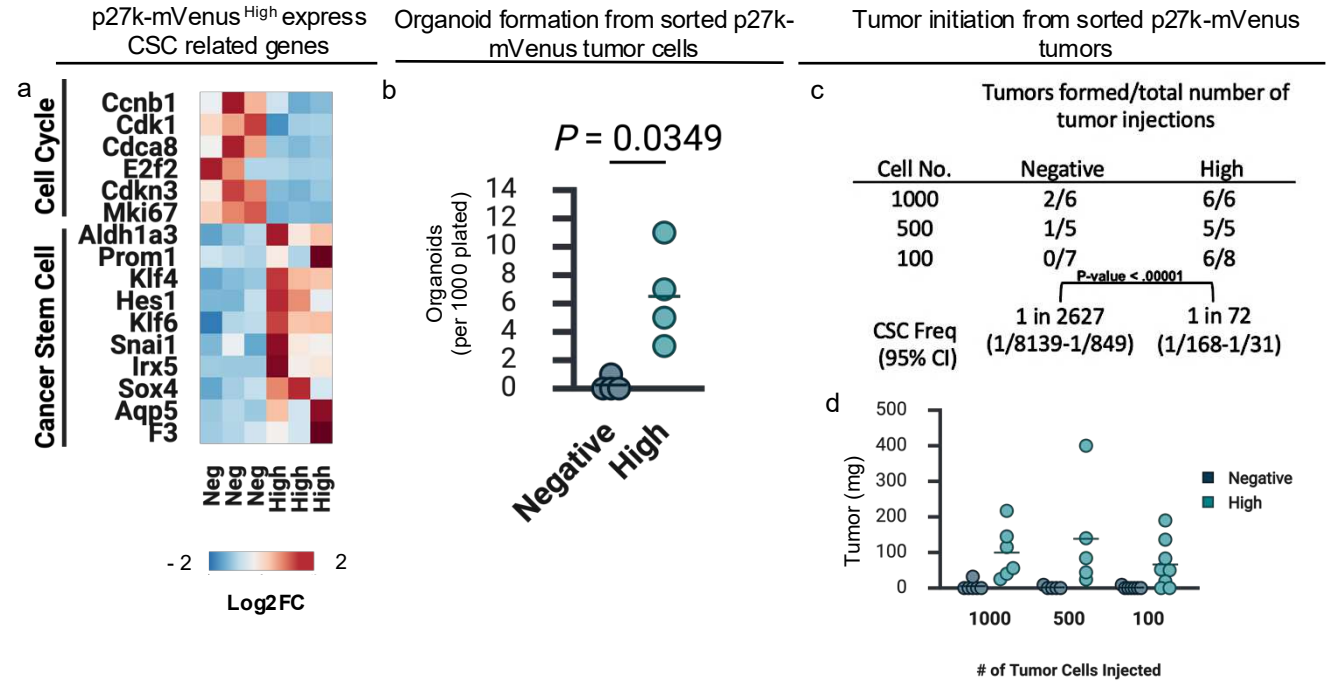

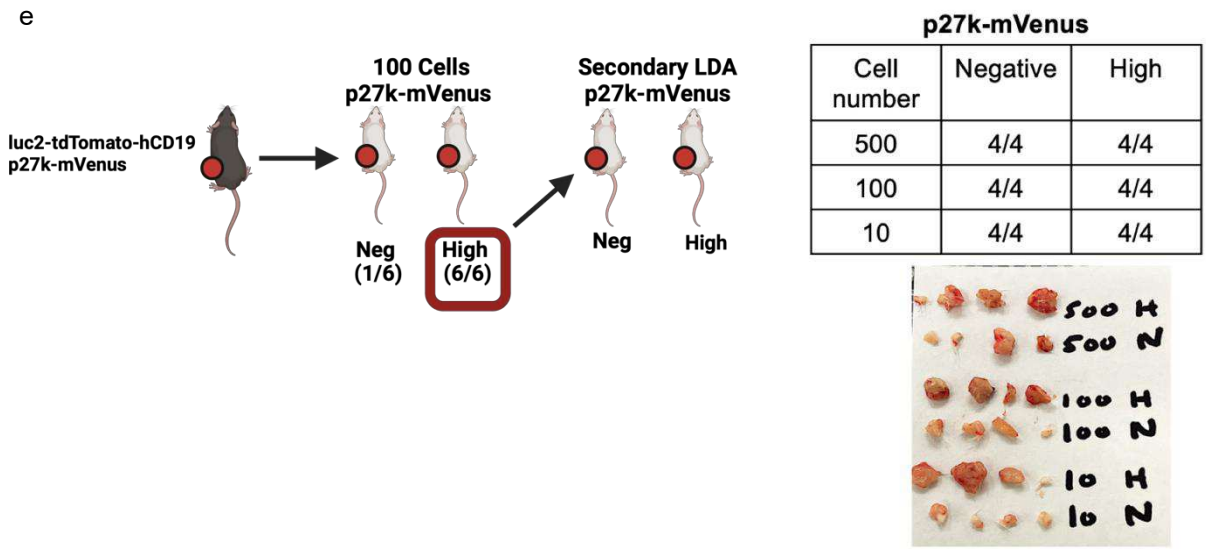

Figure 5. Quiescent cancer cells exhibit functional cancer stem cell properties. a, Heatmap of differentially expressed genes related to cell cycle regulation and cancer stem cell (CSC) signatures in p27k-mVenus ^{Negative} (Neg) and ^{High} (High) cells from three independent experiments ($n = 3$). **b**, Organoid formation efficiency shown as number of organoids per 1,000 cells plated ($n = 4$ independent experiments).**c**, Tumor-initiating capacity presented as the number of tumors formed per total injections following limiting dilution. CSC frequency was calculated using a chi-square goodness-of-fit test. **d**, Tumor weights from mice injected with p27k-mVenus Negative or High cells at 100, 500, or 1,000 cells per injection. Data are presented as mean tumor weight ± s.e.m. **e**, Summary of tumors formed per injection in secondary limiting dilution assays. All statistical analyses, except panel **c**, were performed using unpaired two-tailed *t*-tests. All figures and illustrations were created in https://BioRender.com.

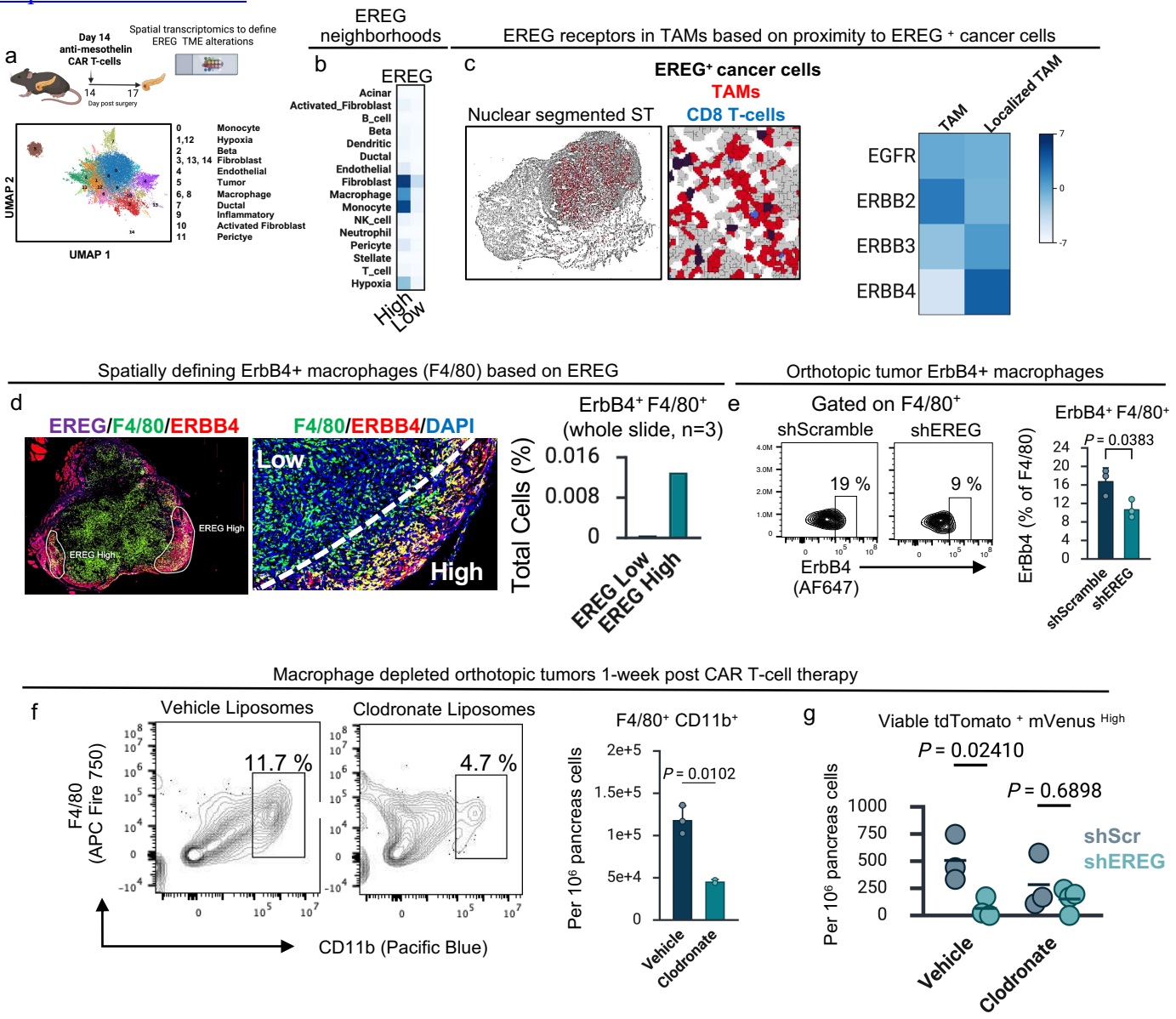

Figure 6. ErbB4 expressing tumor associated macrophages are spatially localized to EREG. a, Schematic of tumor microenvironment evaluation using spatial transcriptomics. Tumors were collected three days post CAR T-cell therapy and analyzed with Visium HD 3' spatial transcriptomics. UMAP plot shows clusters annotated by predicted cell type. **b**, Comparison of predicted cell type enrichment in EREG-high versus EREG-low regions within a murine pancreatic tumor. **c**, Segmented tumor map showing localization of EREG^{+} cancer cells (black), tumor-associated macrophages (TAMs; red), and CD8^{+} T cells (blue). Differential expression of potential EREG receptors (EGFR, ERBB2–4) was analyzed in macrophages proximal to EREG-expressing

cancer cells (localized TAMs) versus bulk TAMs. **d**, Whole-slide immunostaining of orthotopic tumors (n = 3). EREG regions were classified as high or low (purple pseudocolor). Double-stained ErbB4$^+$F4/80$^+$ cells were quantified in each region and normalized to % of total cells using HALO analysis software (iHisto.io). **e**, Flow cytometric quantification of ErbB4$^+$ macrophages (F4/80$^+$) in orthotopic tumors with or without EREG knockdown 7 days post CAR T-cell transfer (n = 3; mean ± SD; unpaired t-test). **f**, Flow cytometry quantification of macrophage depletion post clodronate treatment, expressed as CD11b$^+$F4/80$^+$ cells per million sorted cells (n = 2-3; mean ± SD). **g**, Flow cytometry of mVenus ^{High} cancer cells from vehicle or clodronate-treated tumors one week post CAR T-cell therapy (n = 3). Statistical comparisons used two-way ANOVA with Tukey's test. All figures and illustrations, with exception to contour plots and spatial transcriptomic map, were created in https://BioRender.com.

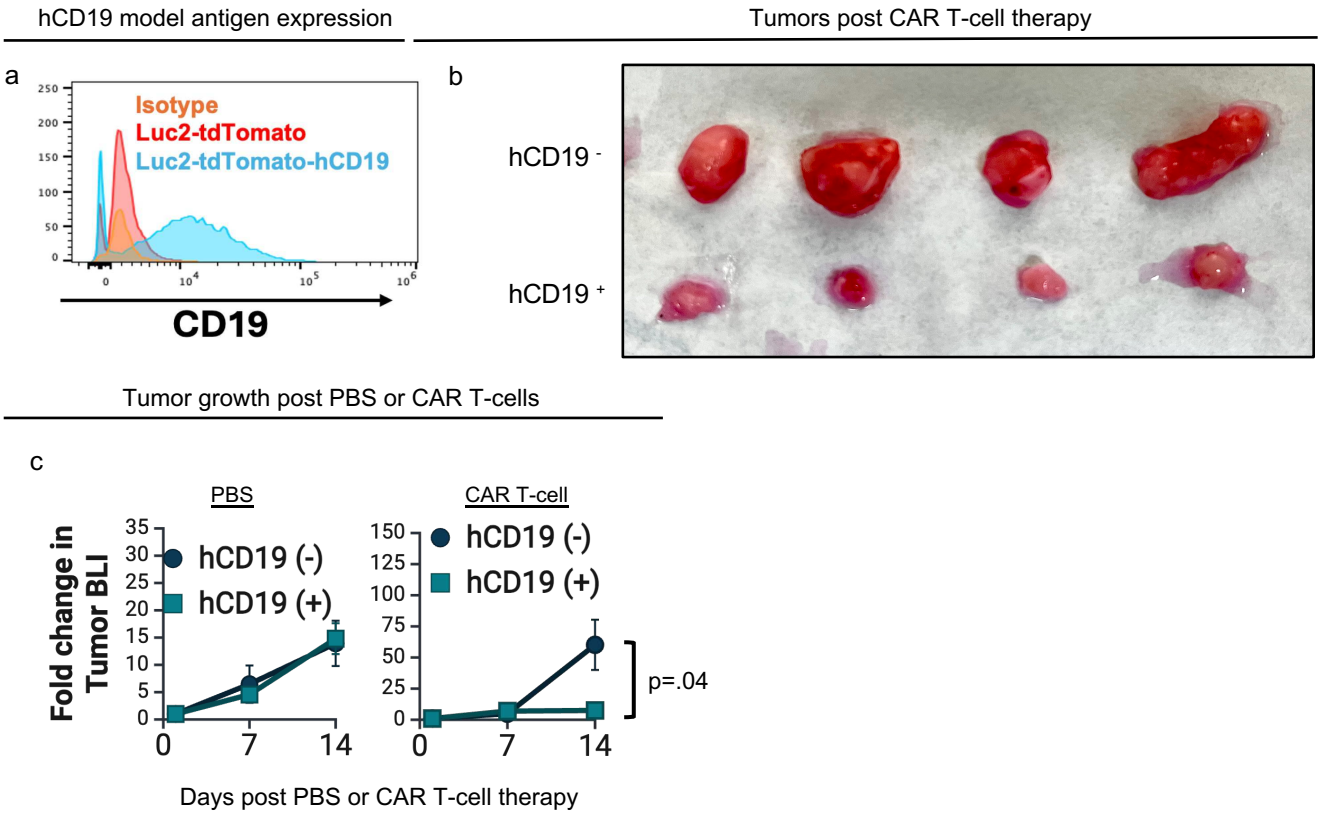

Extended Data Fig. 1. Quiescent (p27k-mVenus high) cells are enriched post-therapy *in vivo*. a, Flow cytometry of mT4-2D cells using isotype-APC or CD19-APC to confirm membrane expression of the model antigen. **b**, Representative images of tumors lacking or expressing hCD19 captured two weeks post CAR T-cell therapy. **c**, Tumor growth monitored by bioluminescence imaging (BLI), expressed as fold change from day 1 (24 h post-implantation) with mean ± SEM (n = 4–5). PBS-treated mice were compared to CAR T-cell–treated mice. Differences between hCD19$^-$ and hCD19$^+$ tumors were assessed by unpaired t-test. Fig. c was created in https://BioRender.com.

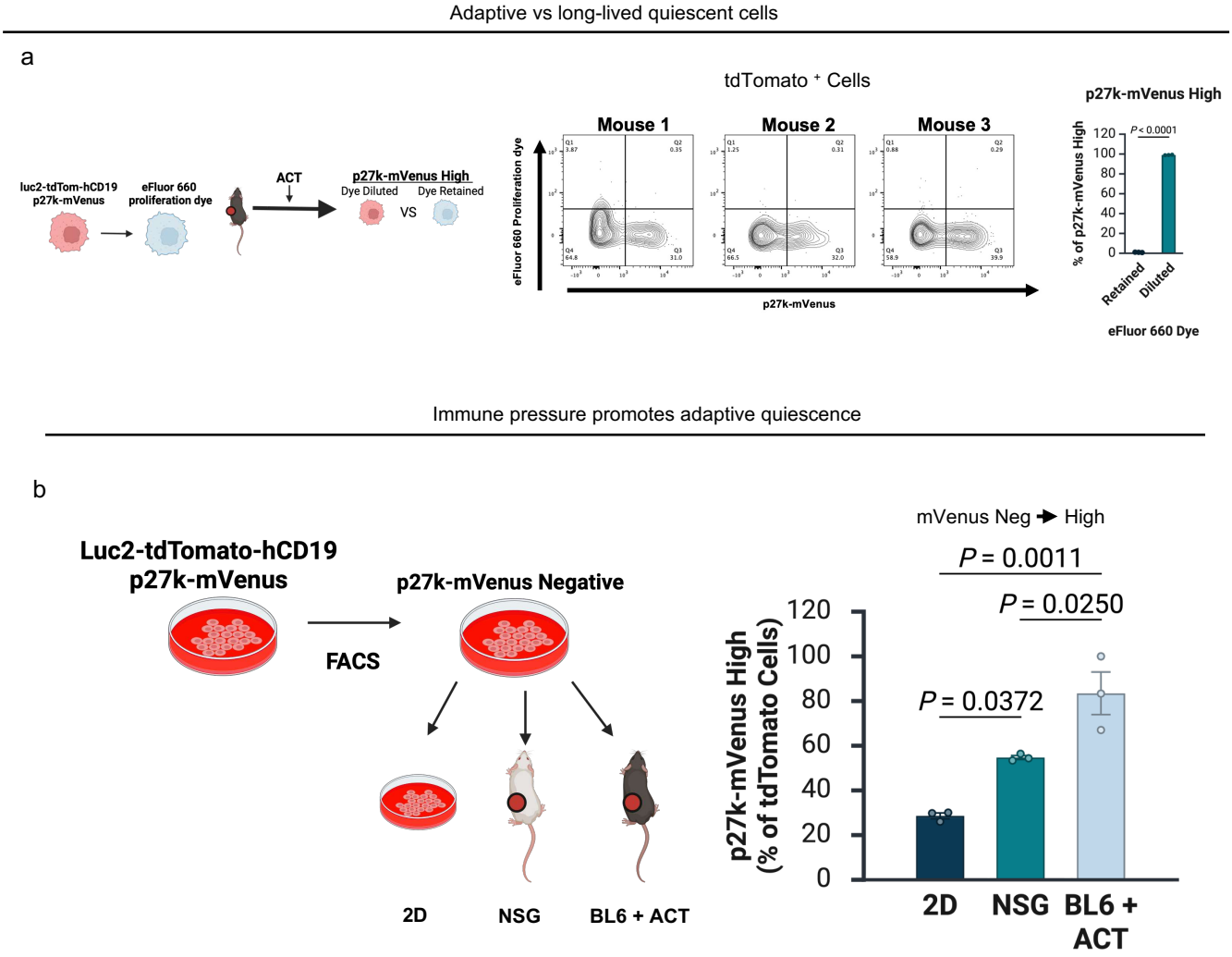

Extended Data Fig. 2. Cancer cells adopt a quiescent state post-therapy. a, Schematic of the experimental design in which quiescent reporter cells were labeled with a proliferative dye, implanted into mice, and treated with CAR T cells (ACT). mVenus expression was analyzed in dye-diluted versus dye-retained populations. Percentage of viable tdTomato^{+} p27k-mVenus ^{High} cells within eFluor 660 low (diluted) versus high (retained) populations. Bars represent mean ± SD (n = 3). Paired t-tests were used for statistical analysis. **b**, Diagram of the experimental setup for *in vivo* and 2D culture comparisons. Percentage of p27k-mVenus ^{High} cells within the viable tdTomato^{+} population across standard 2D culture, NSG tumors, and BL6 + ACT tumors at day 21 post-culture or post-injection. For ACT, five million CAR T cells were administered on day 10. Bars indicate mean ± SEM (n = 3–4). Statistical significance was determined by one-way ANOVA with Tukey's post hoc test. Illustrations and panel **b** were created in https://BioRender.com.

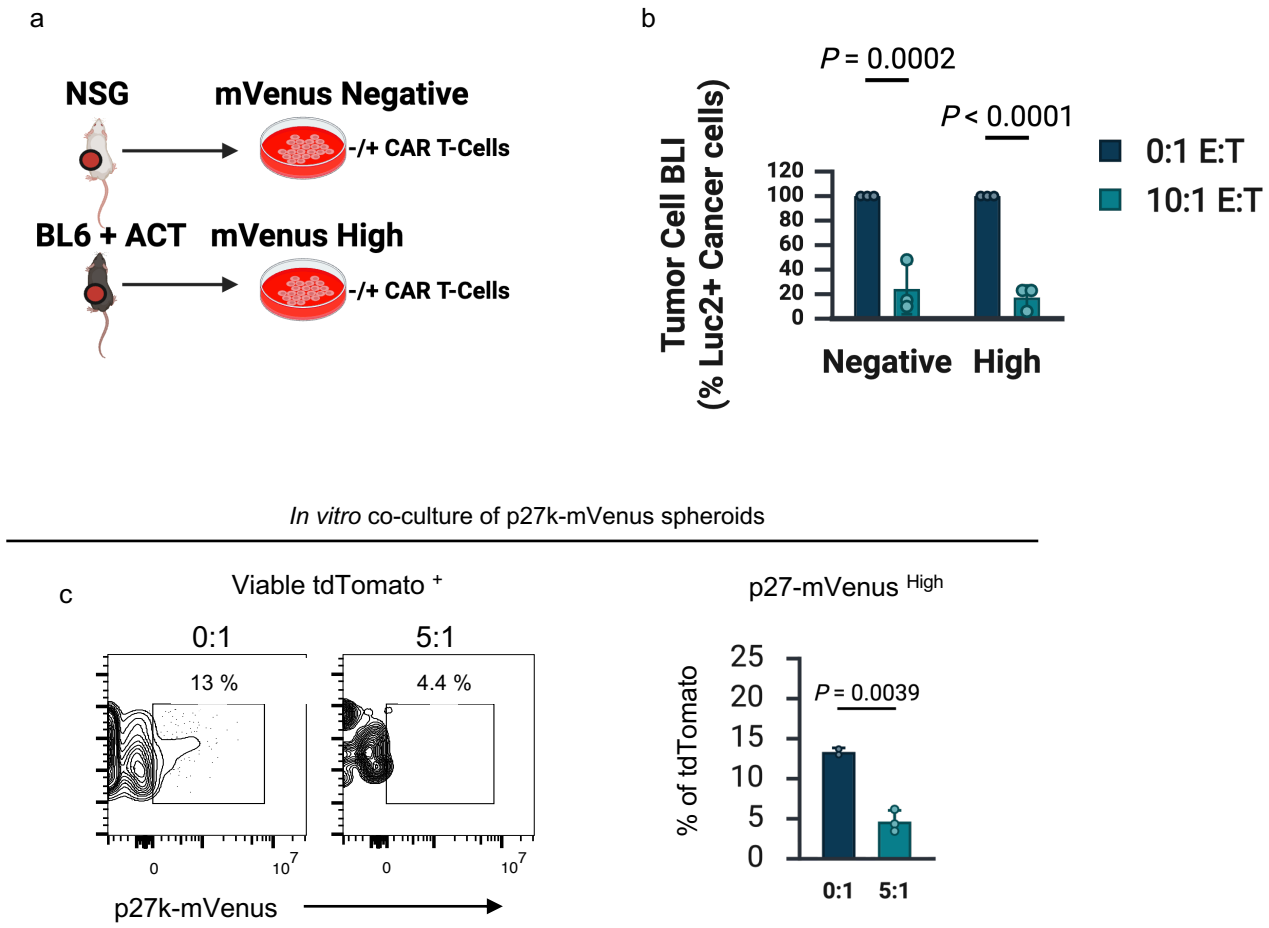

Extended Data Fig. 3. Quiescent cancer cells do not display intrinsic resistance to CAR T-cells *in vitro*. a, Schematic of an *ex vivo* co-culture experiment in which tdTomato^{+} hCD19^{+} FACS-sorted tumor cells were incubated with or without anti-hCD19 CAR T-cells for 48 hours at a 10:1 effector-to-target (E:T) ratio. Viable tumor cells were quantified by luciferase bioluminescence (BLI). **b**, Tumor cell BLI relative to cells grown without T cells. Bars represent mean ± SEM (n = 3). Statistical significance was determined using two-way ANOVA with Tukey's multiple comparisons test. **c**, Flow cytometry analysis 48 hours post co-culture of cancer spheroids with or without CAR T cells at 0:1 (n = 2) or 5:1 E:T (n = 3). Cells were gated as viable (zombie aqua^{-}), and the percentage of mVenus ^{High} cells within the tdTomato^{+} population was quantified. Bars represent mean ± SEM. Statistical comparisons were performed using an unpaired two-tailed t-test. All graphs and illustrations were created in https://BioRender.com.

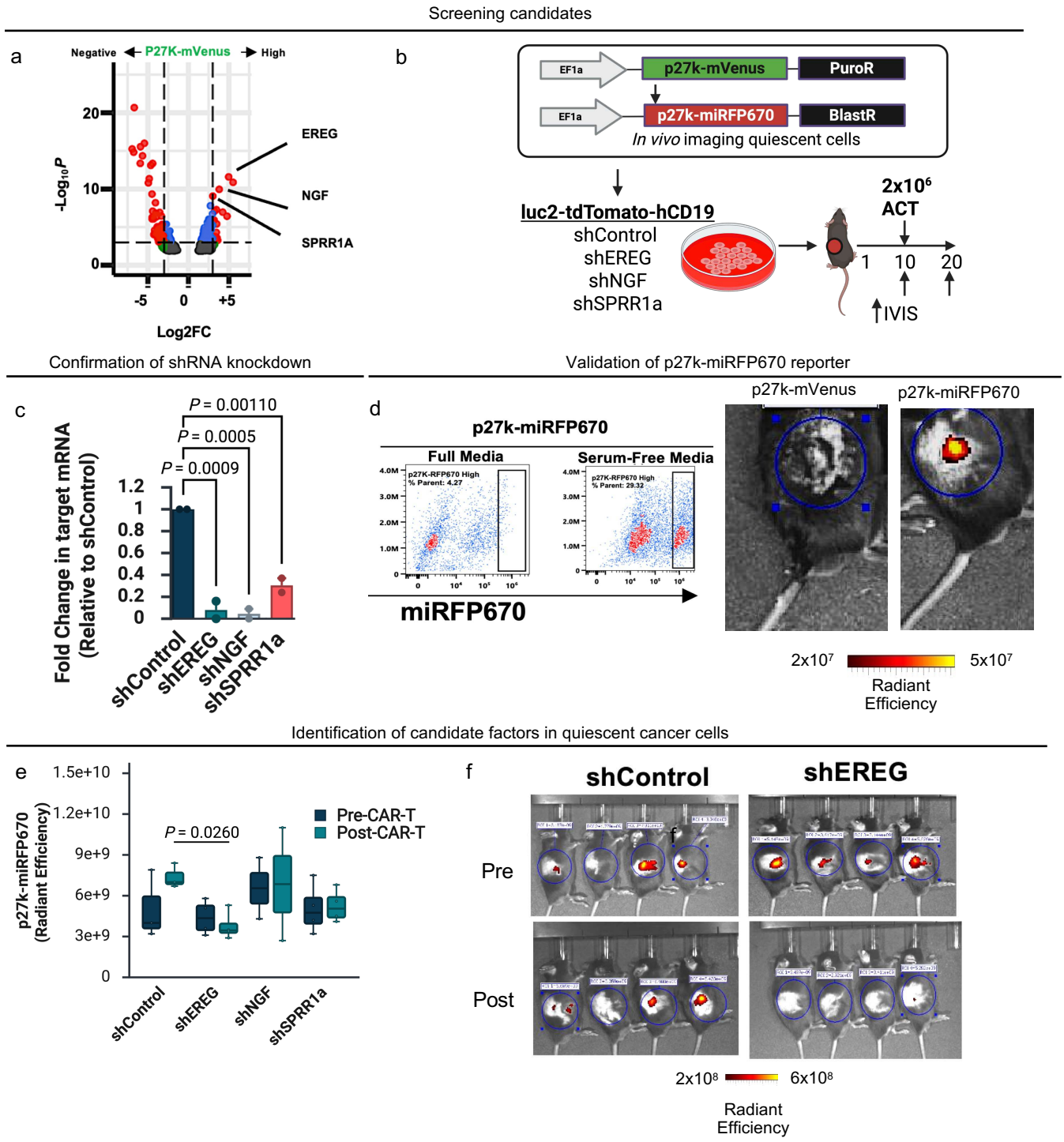

Extended Data Fig. 4. Identification of candidate factors in quiescent cancer cells. a, Volcano plot showing the most differentially expressed genes (absolute $\log_2$ fold change ≥ 4, adjusted $p < 0.01$) between p27k-mVenus ^{Negative} and mVenus ^{High} cell populations. **b**, Schematic of the experimental workflow using a modified quiescent reporter (p27k-miRFP670) for real-time visualization of quiescent cells (Ref. [67]) in S.C. tumors

following knockdown of the top three candidate factors identified by RNA-seq between mVenus ^{Negative} and mVenus ^{High} cells. **c**, Quantification of target gene knockdown using RNAi constructs relative to shControl. Values are mean ± SD from two independent experiments (n = 2). d, Flow cytometry validation of the live-cell quiescent reporter after 48 hours of serum starvation. IVIS imaging of S.C. tumors including background controls (tdTomato-luc2; p27k-mVenus) and tumors expressing the modified p27k-miRFP670 reporter with tdTomato-luc2.**e**, Measurement of miRFP670 expression in vivo before (pre-ACT) and ten days after CAR T-cell therapy (post-ACT). Box plots show mean ± SD for shControl (n = 3), shEREG (n = 4), shNGF (n = 2), and shSPRR1a (n = 4). Statistical significance was assessed using two-way ANOVA with Dunnett's multiple comparisons. **f**, Representative IVIS images of miRFP670 signals in shControl and shEREG tumor-bearing mice pre- and post-CAR T-cell therapy. All graphs and illustrations were created in https://BioRender.com.

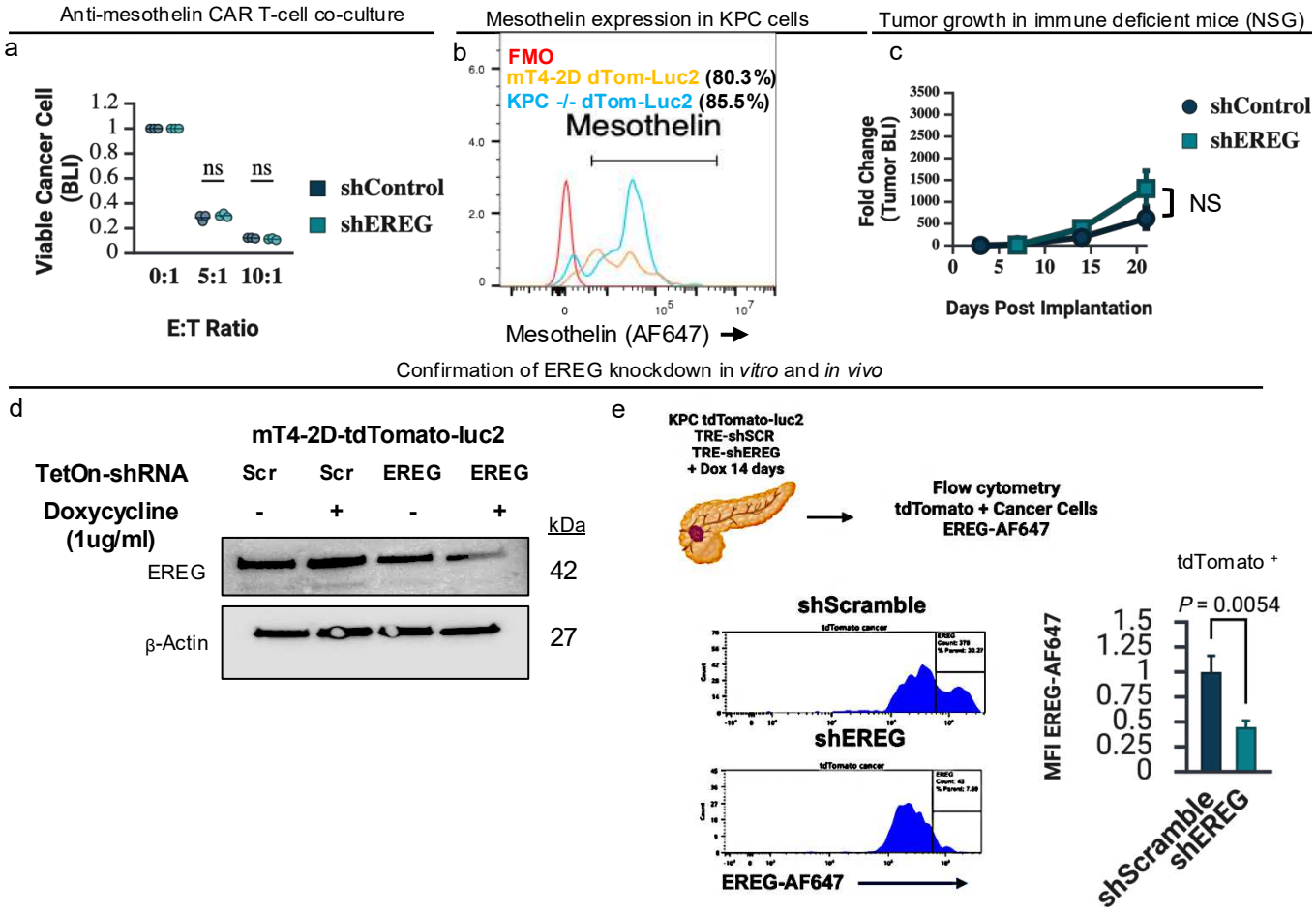

Extended Data Fig. 5. EREG is involved in CAR T-cell therapy responses. a, Viable shControl and shEREG mT4-2D cells were quantified 48 hours after co-culture with anti-mesothelin CAR T cells at effector-to-target ratios of 5:1 or 10:1 using luciferase expression. **b**, Flow cytometry measurement of membrane-bound mesothelin (mesothelin-APC) with a fluorescent minus one (FMO) control included. **c**, Relative tumor growth of shControl and shEREG cancer cells in NSG mice, measured by bioluminescence imaging three days after subcutaneous implantation. Data represent mean ± SEM (n = 6–7). **d**, Western blot analysis of EREG expression with Beta Actin as a loading control. Uncropped blots are included in the Supplementary Information. **e**, *In vivo* validation of EREG knockdown by flow cytometry two weeks after doxycycline administration. Pancreatic tumors were digested, and tdTomato$^+$ cancer cells were analyzed for EREG levels in TetOn-shScramble and TetOn-shEREG tumors. Doxycycline was provided for ten days prior to analysis. Data

are shown as mean ± SD (n = 3; unpaired t-test). All graphs and illustrations were created in https://BioRender.com.

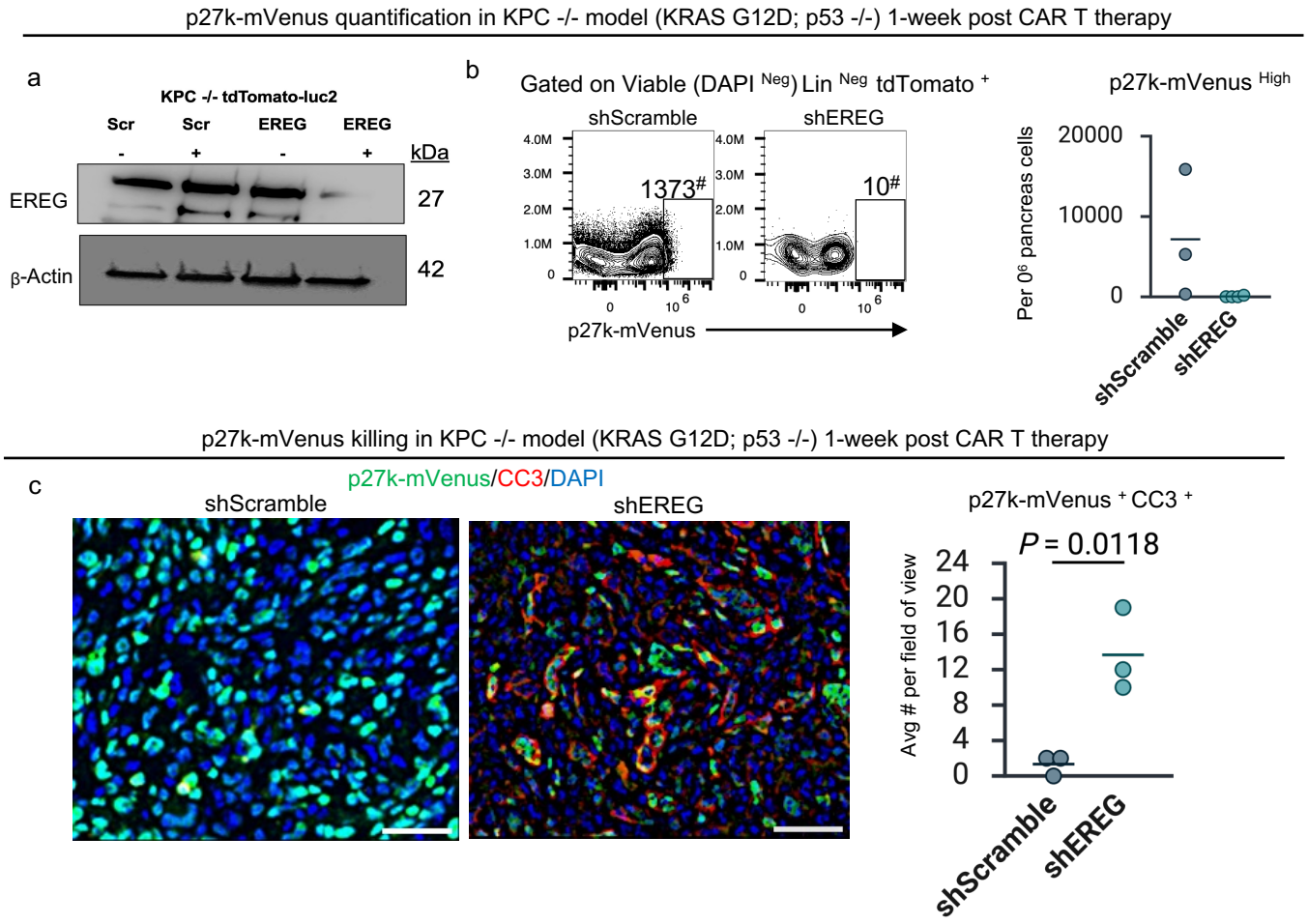

Extended Data Fig. 6. Effect of EREG knockdown in the KPC -/- model. a, Western blot confirming EREG knockdown in KPC$^{-/-}$ cancer cells. Full, uncropped blots are provided in the Supplementary Information. **b**, Quantification of quiescent cancer cells in KPC $^{-/-}$ orthotopic tumors one week post CAR T-cell therapy, comparing TetOn-shEREG and TetOn-shScramble tumors. Contour plots represent the frequency (number, #) of mVenus ^{High} cells within viable (DAPI ^{Neg}), lineage cocktail negative (Lin ^{Neg}), tdTomato $^{+}$ cells. Dot plot represents mVenus ^{High} cells per 10^6 viable cells sorted (n=3 per group; unpaired t-test). **c**, Immunofluorescence staining of TetOn-shScramble and TetOn-shEREG KPC $^{-/-}$ orthotopic tumors one week after CAR T-cell therapy. Sections were stained for GFP (mVenus) and cleaved caspase-3 (CC3) with DAPI counterstaining. Graph shows the mean number of mVenus^{+}CC3^{+} cells per field across 3–4 fields per section from three independent tumors (n = 3; unpaired t-test). All graphs and illustrations were created in https://BioRender.com.

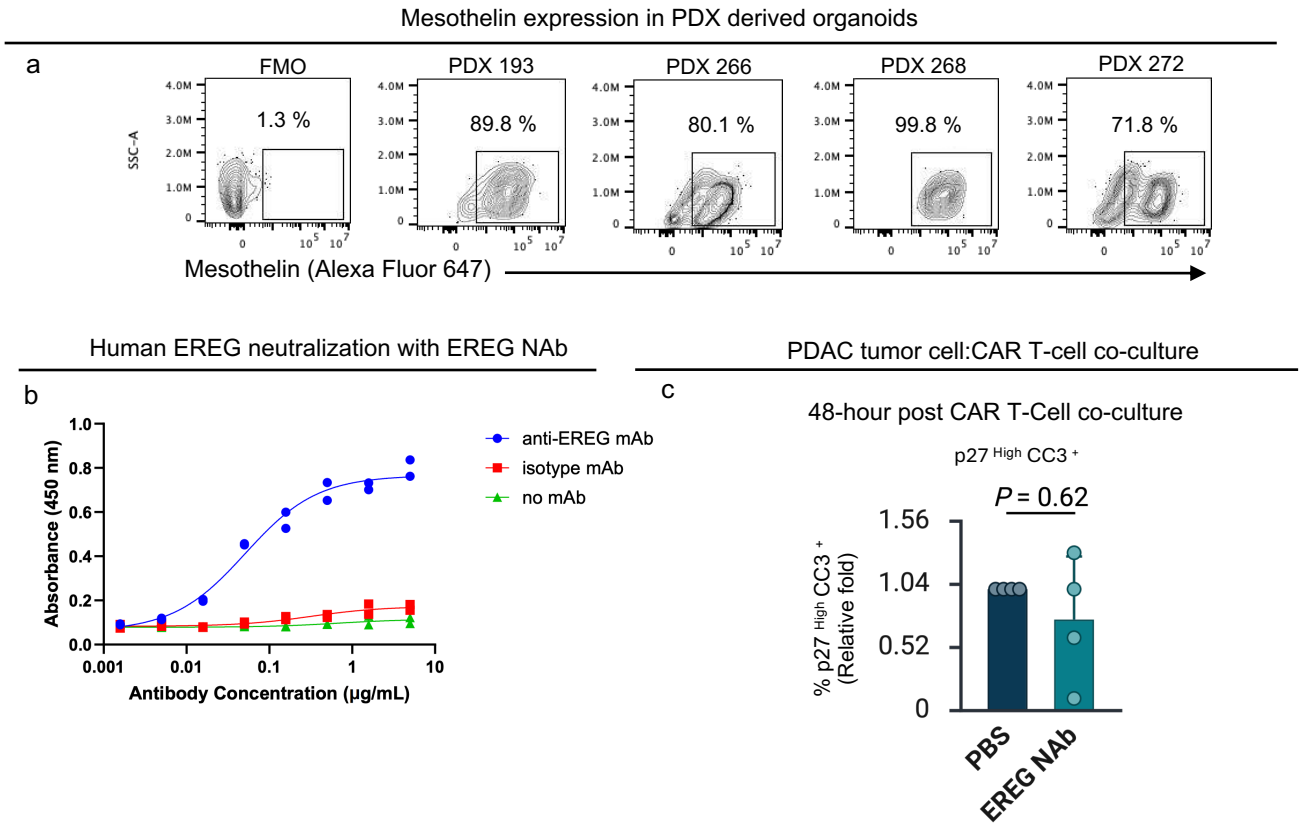

Extended Fig. 7. Effect of EREG inhibition in human PDAC a, Flow cytometry analysis of PDX cancer cells for mesothelin expression (Alexa Fluor 647). A fluorescent minus one (FMO) control was used to set gating. **b**, Quantification of EREG binding by ELISA. Isotype (isotype mAb) and no-antibody (no mAb) controls were included. **c**, Quantification of p27 ^{High} cell killing in PDX cancer cells co-cultured directly with CAR T cells, as described in Fig. 4f. Data represent mean ± SD (n = 4). Statistical significance was determined using the two-tailed Mann–Whitney U test. Panel **c** was created in https://BioRender.com.

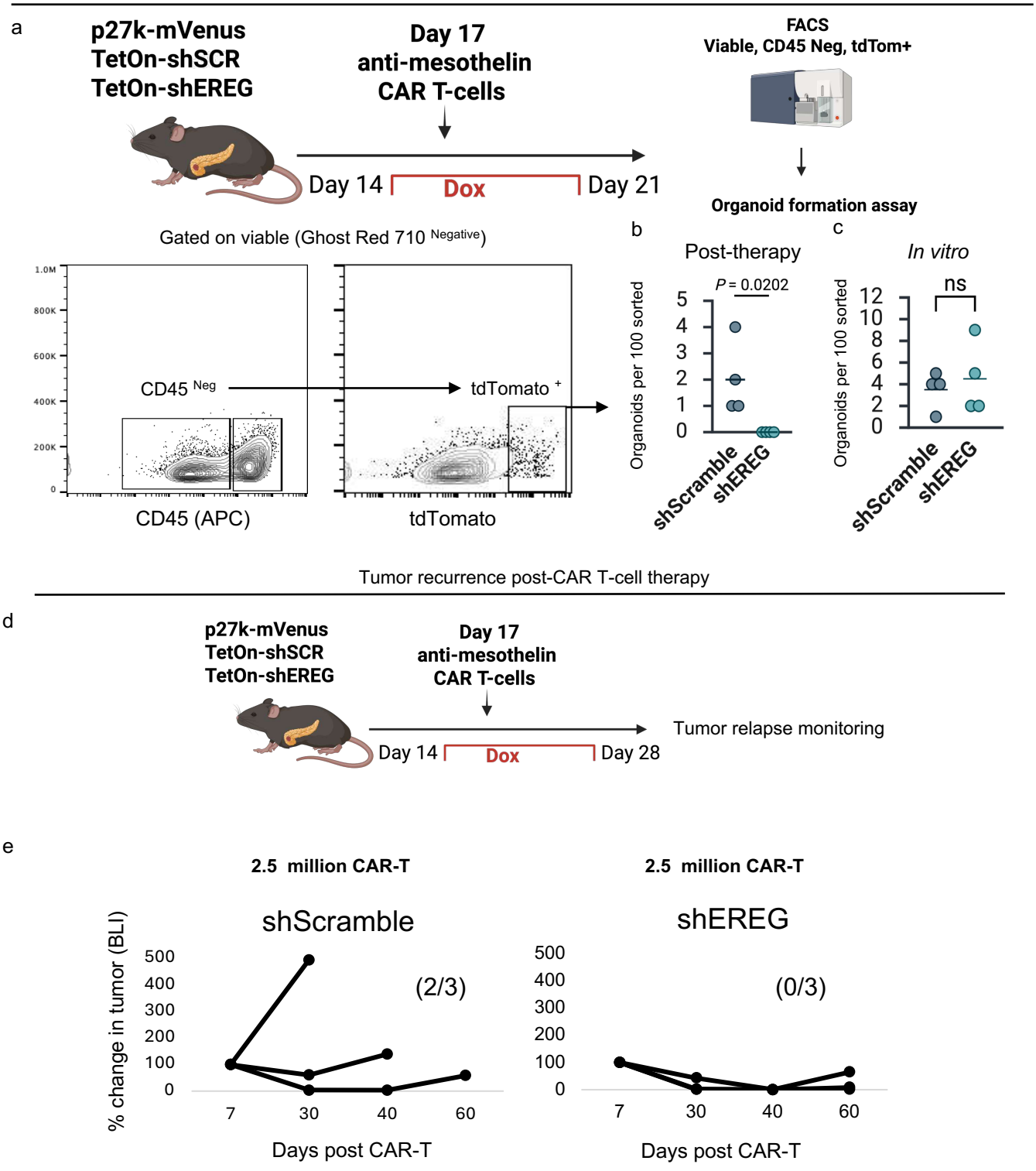

Extended Data Fig. 8. Quiescent cancer cells eliminated by EREG inhibition exhibit stem-like, tumor-propagating properties. a, Schematic of the experimental setup. **b**, tdTomato$^+$, CD45$^-$ cancer cells sorted from TetOn-shScramble or TetOn-shEREG pancreatic tumors one week post CAR T-cell therapy. Graph shows mean organoids formed per 100 cells from three mice (n = 3; unpaired t-test). **c**, shScramble and EREG knockdown

cells were cultured with doxycycline for ten days *in vitro*. Cells (tdTomato^{+}, CD45^{-}) were sorted directly into Matrigel-coated plates to assess organoid formation. Graph shows mean organoids formed per 100 cells from three independent experiments ($n = 3$; unpaired *t*-test). **d**, Schematic of the experimental design for tumor relapse studies. **e**, Tumor relapse following administration of 2.5×10^6 CAR T-cells. Graph shows tumor bioluminescence imaging (BLI) ± SEM for control (shScramble, $n = 3$) and EREG knockdown (shEREG, $n = 3$) tumors, expressed as a relative % change to week 1 BLI. All graphs and schematics were created in https://BioRender.com.

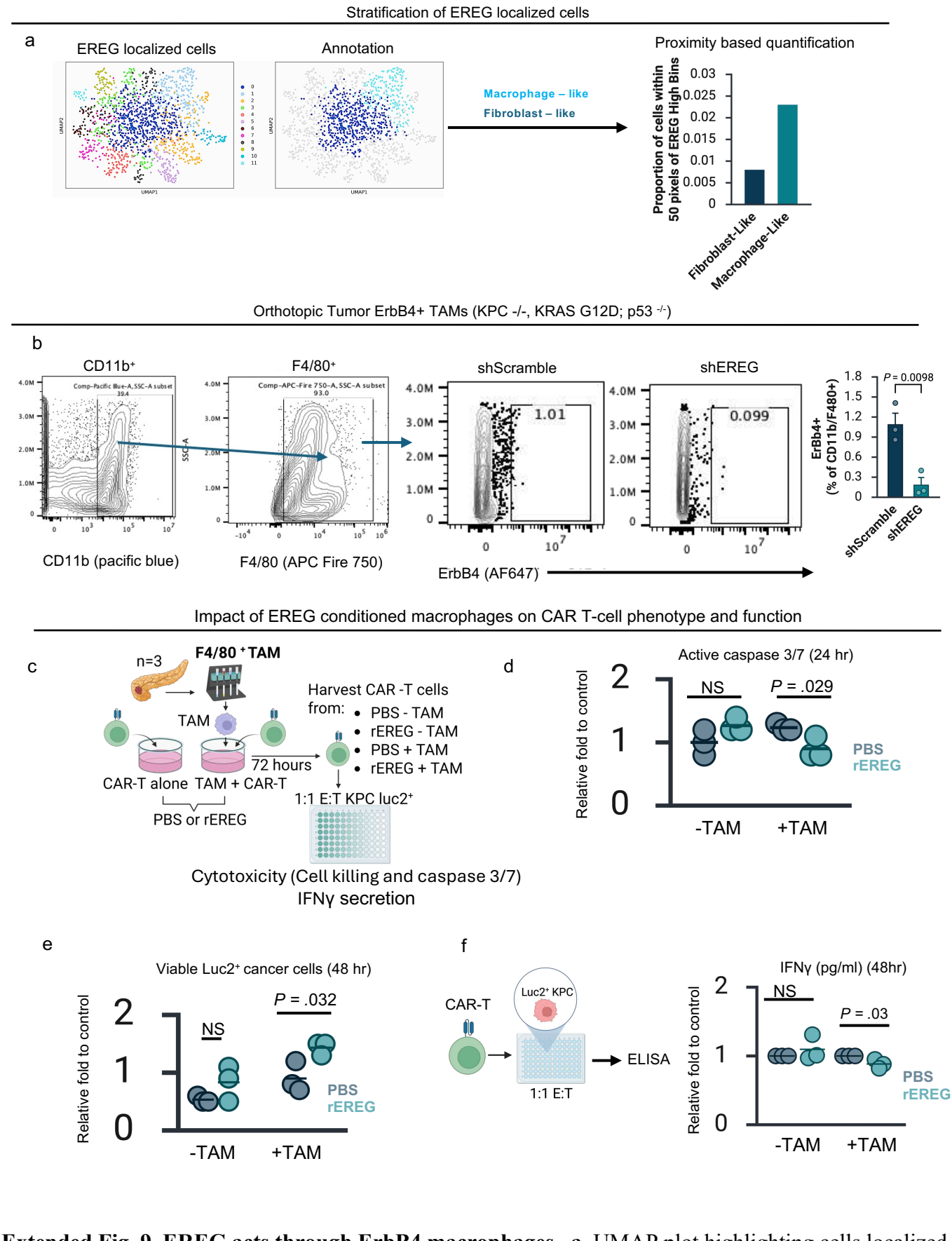

Extended Fig. 9. EREG acts through ErbB4 macrophages. **a**, UMAP plot highlighting cells localized within EREG-high microenvironments. Cells were classified as macrophage-like or fibroblast-like based on gene marker expression. Graph quantifies the number of macrophage-like versus fibroblast-like cells located within 50 pixels of EREG microenvironment hotspots. **b**, Flow cytometry analysis of ErbB4+ cells (Alexa Fluor 647)

from KPC$^{-/-}$ orthotopic tumors. **c**, Schematic of the experimental design. **d**, Active caspase 3/7 activity measured one hour after addition of CellEvent Green, 24 hours post co-culture with CAR T-cells under the indicated pre-exposure conditions. Data are expressed as relative fold change of fluorescent units (RFU) compared to PBS (-) TAM condition. **e**, Quantification of viable tumor cells 48 hours post co-culture with CAR T-cells using luciferase (relative luciferase units, RLU). Graph shows fold change relative to cancer cells cultured without T-cells. **f**, IFNγ ELISA quantification expressed as relative fold change compared to PBS (-/+) TAM. Data in panels d–f are from three independent experiments (n = 3; unpaired t-test). All graphs and illustrations were created in https://BioRender.com.

References

1. Siegel, R.L., et al., *Cancer statistics, 2023.* CA Cancer J Clin, 2023. **73**(1): p. 17-48.
2. Zhao, K., et al., *Neoadjuvant Pembrolizumab Enables Successful Downstaging and Resection of Borderline Resectable MSI-H/dMMR Pancreatic Ductal Adenocarcinoma: A Case Report and Literature Review.* Journal of Gastrointestinal Cancer, 2025. **56**(1): p. 112.
3. Chakrabarti, S., et al., *Detection of microsatellite instability-high (MSI-H) by liquid biopsy predicts robust and durable response to immunotherapy in patients with pancreatic cancer.* Journal for immunotherapy of cancer, 2022. **10**(6): p. e004485.
4. Beatty, G.L., et al., *Mesothelin-specific chimeric antigen receptor mRNA-engineered T cells induce antitumor activity in solid malignancies.* Cancer immunology research, 2014. **2**(2): p. 112-120.
5. Aznar, M.A., et al., *Clinical and molecular dissection of CAR T cell resistance in pancreatic cancer.* Cell Reports Medicine, 2025.
6. Bayne, L.J., et al., *Tumor-derived granulocyte-macrophage colony-stimulating factor regulates myeloid inflammation and T cell immunity in pancreatic cancer.* Cancer cell, 2012. **21**(6): p. 822-835.
7. Zhu, Y., et al., *Tissue-resident macrophages in pancreatic ductal adenocarcinoma originate from embryonic hematopoiesis and promote tumor progression.* Immunity, 2017. **47**(2): p. 323-338. e6.
8. Zuo, C., et al., *Stromal and therapy-induced macrophage proliferation promotes PDAC progression and susceptibility to innate immunotherapy.* Journal of Experimental Medicine, 2023. **220**(6): p. e20212062.
9. Wang, W., et al., *RIP1 kinase drives macrophage-mediated adaptive immune tolerance in pancreatic cancer.* Cancer cell, 2018. **34**(5): p. 757-774.
10. Kaneda, M.M., et al., *Macrophage PI3Kγ drives pancreatic ductal adenocarcinoma progression.* Cancer discovery, 2016. **6**(8): p. 870-885.
11. Yu, J., et al., *Liver metastasis restrains immunotherapy efficacy via macrophage-mediated T cell elimination.* Nature medicine, 2021. **27**(1): p. 152-164.
12. Pascual-García, M., et al., *LIF regulates CXCL9 in tumor-associated macrophages and prevents CD8+ T cell tumor-infiltration impairing anti-PD1 therapy.* Nature communications, 2019. **10**(1): p. 2416.
13. Rodriguez-Garcia, A., et al., *CAR-T cell-mediated depletion of immunosuppressive tumor-associated macrophages promotes endogenous antitumor immunity and augments adoptive immunotherapy.* Nature communications, 2021. **12**(1): p. 877.
14. Li, J.H., et al., *IQGAP1 maintains pancreatic ductal adenocarcinoma clonogenic growth and metastasis.* Pancreas, 2019. **48**(1): p. 94-98.
15. Bailey, J.M., et al., *DCLK1 marks a morphologically distinct subpopulation of cells with stem cell properties in preinvasive pancreatic cancer.* Gastroenterology, 2014. **146**(1): p. 245-256.
16. Rasheed, Z., Q. Wang, and W. Matsui, *Isolation of stem cells from human pancreatic cancer xenografts.* Journal of visualized experiments: JoVE, 2010(43): p. 2169.
17. Wang, V.M.-Y., et al., *CD9 identifies pancreatic cancer stem cells and modulates glutamine metabolism to fuel tumour growth.* Nature cell biology, 2019. **21**(11): p. 1425-1435.
18. Xie, X.P., et al., *Quiescent human glioblastoma cancer stem cells drive tumor initiation, expansion, and recurrence following chemotherapy.* Developmental Cell, 2022. **57**(1): p. 32-46. e8.

19. Chen, M., R.R. Reed, and A.P. Lane, *Chronic inflammation directs an olfactory stem cell functional switch from neuroregeneration to immune defense.* Cell stem cell, 2019. **25**(4): p. 501-513. e5.
20. Li, R., et al., *A proinflammatory stem cell niche drives myelofibrosis through a targetable galectin-1 axis.* Science translational medicine, 2024. **16**(768): p. eadj7552.
21. Liu, C., et al., *Niche inflammatory signals control oscillating mammary regeneration and protect stem cells from cytotoxic stress.* Cell Stem Cell, 2024. **31**(1): p. 89-105. e6.
22. Marqués-Torrejón, M.Á., et al., *Cyclin-dependent kinase inhibitor p21 controls adult neural stem cell expansion by regulating Sox2 gene expression.* Cell stem cell, 2013. **12**(1): p. 88-100.
23. Chakkalakal, J.V., et al., *The aged niche disrupts muscle stem cell quiescence.* Nature, 2012. **490**(7420): p. 355-360.
24. Cheng, T., et al., *Hematopoietic Stem Cell Quiescence Maintained by p21^{cip1/waf1}.* Science, 2000. **287**(5459): p. 1804-1808.
25. Pommier, A., et al., *Unresolved endoplasmic reticulum stress engenders immune-resistant, latent pancreatic cancer metastases.* Science, 2018. **360**(6394): p. eaao4908.
26. Malladi, S., et al., *Metastatic latency and immune evasion through autocrine inhibition of WNT.* Cell, 2016. **165**(1): p. 45-60.
27. Michelatti, D., et al., *Oncogenic enhancers prime quiescent metastatic cells to escape NK immune surveillance by eliciting transcriptional memory.* Nature communications, 2024. **15**(1): p. 2198.
28. Wang, Z., et al., *TGFβ induces an atypical EMT to evade immune mechanosurveillance in lung adenocarcinoma dormant metastasis.* Nature Cancer, 2026: p. 1-19.
29. Miao, Y., et al., *Adaptive immune resistance emerges from tumor-initiating stem cells.* Cell, 2019. **177**(5): p. 1172-1186. e14.
30. Wang, C., et al., *CD276 expression enables squamous cell carcinoma stem cells to evade immune surveillance.* Cell stem cell, 2021. **28**(9): p. 1597-1613. e7.
31. Odell, I.D., et al., *Epiregulin is a dendritic cell–derived EGFR ligand that maintains skin and lung fibrosis.* Science immunology, 2022. **7**(78): p. eabq6691.
32. Oki, T., et al., *A novel cell-cycle-indicator, mVenus-p27K−, identifies quiescent cells and visualizes G0–G1 transition.* Scientific reports, 2014. **4**(1): p. 4012.
33. Baldominos, P., et al., *Quiescent cancer cells resist T cell attack by forming an immunosuppressive niche.* Cell, 2022. **185**(10): p. 1694-1708. e19.
34. Zhang, Y., et al., *Important role of epiregulin in inflammatory responses during corneal epithelial wound healing.* Investigative ophthalmology & visual science, 2012. **53**(4): p. 2414-2423.
35. Lee, D., et al., *Epiregulin is not essential for development of intestinal tumors but is required for protection from intestinal damage.* Molecular and cellular biology, 2004. **24**(20): p. 8907-8916.
36. Inatomi, O., et al., *Regulation of amphiregulin and epiregulin expression in human colonic subepithelial myofibroblasts.* International journal of molecular medicine, 2006. **18**(3): p. 497-503.
37. Shirasawa, S., et al., *Dermatitis due to epiregulin deficiency and a critical role of epiregulin in immune-related responses of keratinocyte and macrophage.* Proceedings of the National Academy of Sciences, 2004. **101**(38): p. 13921-13926.
38. Zhao, Y.-C., et al., *Epiregulin enhances periodontal tissue regeneration by promoting bone marrow mesenchymal stem cell functions under inflammatory niches.* World Journal of Stem Cells, 2026. **18**(2).
39. Li, A., et al., *A novel immunogenomic signature to predict prognosis and reveal immune infiltration characteristics in pancreatic ductal adenocarcinoma.* Precision Clinical Medicine, 2022. **5**(2): p. pbac010.
40. Hingorani, S.R., et al., *Trp53R172H and KrasG12D cooperate to promote chromosomal instability and widely metastatic pancreatic ductal adenocarcinoma in mice.* Cancer cell, 2005. **7**(5): p. 469-483.
41. Boj, S.F., et al., *Organoid models of human and mouse ductal pancreatic cancer.* Cell, 2015. **160**(1): p. 324-338.
42. Chowdhury, P.S., et al., *Isolation of a high-affinity stable single-chain Fv specific for mesothelin from DNA-immunized mice by phage display and construction of a recombinant immunotoxin with anti-tumor activity.* Proceedings of the National Academy of Sciences, 1998. **95**(2): p. 669-674.

43. Shiraiwa, H., et al., *Humanized anti-epiregulin antibody, and cancer therapeutic agent comprising said antibody as active ingredient*. 2017, Google Patents.
44. Hu, Y. and G.K. Smyth, *ELDA: extreme limiting dilution analysis for comparing depleted and enriched populations in stem cell and other assays.* Journal of immunological methods, 2009. **347**(1-2): p. 70-78.
45. McClellan, B., et al., *Flotillin-1 palmitoylation is essential for its stability and subsequent tumor promoting capabilities.* Oncogene, 2024. **43**(14): p. 1063-1074.
46. Chen, E.Y., et al., *Enrichr: interactive and collaborative HTML5 gene list enrichment analysis tool.* BMC Bioinformatics, 2013. **14**(1): p. 128.
47. Wolf, F.A., P. Angerer, and F.J. Theis, *SCANPY: large-scale single-cell gene expression data analysis.* Genome biology, 2018. **19**(1): p. 15.
48. Palla, G., et al., *Squidpy: a scalable framework for spatial omics analysis.* Nature methods, 2022. **19**(2): p. 171-178.
49. Virshup, I., et al., *anndata: Access and store annotated data matrices.* Journal of Open Source Software, 2024. **9**(101): p. 4371.
50. Traag, V.A., L. Waltman, and N.J. Van Eck, *From Louvain to Leiden: guaranteeing well-connected communities.* Scientific reports, 2019. **9**(1): p. 1-12.
51. Fernández, Á., et al., *A single-cell atlas of the murine pancreatic ductal tree identifies novel cell populations with potential implications in pancreas regeneration and exocrine pathogenesis.* Gastroenterology, 2024. **167**(5): p. 944-960. e15.
52. Ram, P. and K. Sinha. *Revisiting kd-tree for nearest neighbor search*. in *Proceedings of the 25th acm sigkdd international conference on knowledge discovery & data mining*. 2019.
53. Tosi, S., *Matplotlib for Python developers*. Vol. 307. 2009: Packt Publishing Birmingham, UK.
54. Wang, J., et al., *Orthotopic and heterotopic murine models of pancreatic cancer exhibit different immunological microenvironments and different responses to immunotherapy.* Frontiers in Immunology, 2022. **13**: p. 863346.
55. Hu, J., et al., *STING inhibits the reactivation of dormant metastasis in lung adenocarcinoma.* Nature, 2023. **616**(7958): p. 806-813.
56. Roesch, A., et al., *A temporarily distinct subpopulation of slow-cycling melanoma cells is required for continuous tumor growth.* Cell, 2010. **141**(4): p. 583-594.
57. Lim, H.Y.G., et al., *AQP5: A functional gastric cancer stem cell marker in mouse and human tumors.* Science, 2025. **390**(6779): p. eadr2428.
58. Schumacher, M.A., et al., *NRG4-ErbB4 signaling represses proinflammatory macrophage activity.* American Journal of Physiology-Gastrointestinal and Liver Physiology, 2021. **320**(6): p. G990-G1001.
59. Erickson, H.L., et al., *Cancer stem cells release interleukin-33 within large oncosomes to promote immunosuppressive differentiation of macrophage precursors.* Immunity, 2024. **57**(8): p. 1908-1922. e6.
60. He, X., et al., *Tumor-initiating stem cell shapes its microenvironment into an immunosuppressive barrier and pro-tumorigenic niche.* Cell reports, 2021. **36**(10).
61. Massip-Copiz, M., et al., *Epiregulin (EREG) is upregulated through an IL-1β autocrine loop in Caco-2 epithelial cells with reduced CFTR function.* Journal of cellular biochemistry, 2018. **119**(3): p. 2911-2922.
62. Hsu, D., et al., *Toll-like receptor 4 differentially regulates epidermal growth factor-related growth factors in response to intestinal mucosal injury.* Laboratory investigation, 2010. **90**(9): p. 1295-1305.
63. Wang, C., et al., *Targeting epiregulin in the treatment-damaged tumor microenvironment restrains therapeutic resistance.* Oncogene, 2022. **41**(45): p. 4941-4959.
64. Hardbower, D.M., et al., *EGFR-mediated macrophage activation promotes colitis-associated tumorigenesis.* Oncogene, 2017. **36**(27): p. 3807-3819.
65. Sloan-Lancaster, J., et al., *Evaluation of the safety, pharmacokinetics, pharmacodynamics, and efficacy after single and multiple dosings of LY3016859 in healthy subjects and patients with diabetic nephropathy.* Clinical Pharmacology in Drug Development, 2018. **7**(7): p. 759-772.
66. Varet, H., et al., *SARTools: a DESeq2-and EdgeR-based R pipeline for comprehensive differential analysis of RNA-Seq data.* PloS one, 2016. **11**(6): p. e0157022.

67. Shcherbakova, D.M., et al., *Bright monomeric near-infrared fluorescent proteins as tags and biosensors for multiscale imaging.* Nature communications, 2016. **7**(1): p. 12405.

Supplementary Files

This is a list of supplementary files associated with this preprint. Click to download.

- PDXCharacterisitcs.xlsx
- DifferentiallyexpressedgenesmVenusNegativevsmVenusHigh.xlsx
- Flowcytometrygatingandfullwesternblots.pdf
- supplemenatrymaterialstable.xlsx